

*On the role of pre-existing discontinuities
on the micromechanical behavior of
confined rock samples: a numerical study*

**Ge Gao, Mohamed A. Meguid & Luc
E. Chouinard**

Acta Geotechnica

ISSN 1861-1125

Volume 15

Number 12

Acta Geotech. (2020) 15:3483-3510

DOI 10.1007/s11440-020-01037-0

Your article is protected by copyright and all rights are held exclusively by Springer-Verlag GmbH Germany, part of Springer Nature. This e-offprint is for personal use only and shall not be self-archived in electronic repositories. If you wish to self-archive your article, please use the accepted manuscript version for posting on your own website. You may further deposit the accepted manuscript version in any repository, provided it is only made publicly available 12 months after official publication or later and provided acknowledgement is given to the original source of publication and a link is inserted to the published article on Springer's website. The link must be accompanied by the following text: "The final publication is available at link.springer.com".



On the role of pre-existing discontinuities on the micromechanical behavior of confined rock samples: a numerical study

Ge Gao¹ · Mohamed A. Meguid¹ · Luc E. Chouinard¹

Received: 31 January 2020 / Accepted: 13 July 2020 / Published online: 9 August 2020
© Springer-Verlag GmbH Germany, part of Springer Nature 2020

Abstract

The deformation process and failure mechanism of rock mass with increased density of initial joints subjected to confined stress state are investigated in this study using discrete element method (DEM). A numerical model of standard size granite samples is developed and validated using experimental data for both intact and jointed rocks. The micro-parameters of the rock material are first determined, and the effects of the rock discontinuity on strength, deformability, stress–strain relationship, and failure modes are then investigated at the macro-scale level. Analyses are also performed to examine the tensile and shear crack distributions, fragmentation characteristics, particle kinematics, and energy dissipation to advance the current understanding of the deformation processes and failure mechanisms of jointed rock masses. The microscopic evolutions in the fabric and force anisotropy during loading and distributions of contact forces provide insights into the influence of increasing initial jointing on the macroscopic deformational behavior of the rock. The results show how the deceleration in the growth of fabric and contact force anisotropies develops and confirms that the increase in initial jointing and the associated changes in microstructure can restrain the development of anisotropy, thereby reducing significantly the strength of the rock samples.

Keywords Discrete element method · Fabric evolution and anisotropy · Rock discontinuity · Rock failure processes · Micromechanics

1 Introduction

One of the main characteristics of rock mass is the presence of discontinuities, such as fractures, joints, bedding planes, and faults. These discontinuities can have dominant effects on the deformability and strength of a rock mass. In particular, a discontinuity can have a critical effect on the stability of rock slopes and underground structures. Therefore, for stability analysis of rock slopes or support design of underground excavations, it is of crucial

importance to acquire a thorough understanding of the geometrical and mechanical properties of rock discontinuities.

Laboratory experiments on rock samples are usually performed to understand crack evolution as well as the complex mechanical behavior of joints. Uniaxial compression tests conducted on samples with pre-existing discontinuities [18, 34, 35, 58] revealed that the most significant factors controlling the strength, deformation, and failure mechanism of jointed rock include joint length and density, and joint orientation. However, rock masses are generally subjected to in situ confinement and, therefore, it is important to investigate the effect of pre-existing joint sets on the strength and failure behavior of rock under confining pressure. Brown and Trollope [7] carried out a series of triaxial compression tests under five different confinements on an idealized rock-like material with four arrangements of joint sets orientation. They concluded that the predicted strength was much lower than that of the intact material, except for the case of vertical–horizontal

✉ Mohamed A. Meguid
mohamed.meguid@mcgill.ca

Ge Gao
ge.gao2@mail.mcgill.ca

Luc E. Chouinard
luc.chouinard@mcgill.ca

¹ Civil Engineering and Applied Mechanics, McGill University, 817 Sherbrooke St. W, Montreal, QC H3A 0C3, Canada

orientation. Prudencio and Van Sint [49] performed biaxial compression tests on jointed rock samples and indicated that the geometry of the joint systems, the orientation of the principal stresses, and the ratio between intermediate principal stress and intact material compressive strength have significant effects on the failure modes and strengths of jointed rock masses.

Although laboratory experiments can shed some lights on the significance of joint configuration on the mechanical behavior of jointed rock masses [73], the entire failure progression from crack initiation, propagation, and coalescence up to failure is hard to visualize inside the samples during testing [37, 50]. Moreover, the fracture of some brittle rock materials is very rapid, which makes it difficult to trace the process with currently available monitoring devices [25, 77]. In addition, experimental results are sensitive to sample preparation and boundary conditions; a small change in the contact condition between the sample and loading platen may result in a different failure mode [24]. Therefore, given the mechanical and geometrical complexities of jointed rock blocks, there is a need to develop suitable numerical models that are capable of capturing the progression of fracture growth and the associated material damage.

Continuum (e.g., FEM and FDM) and discontinuum (e.g., DEM) methods are among the main methods used to model rock failure. Continuum methods generally assume continuous, isotropic, homogeneous, and linearly elastic medium. However, jointed rocks are usually heterogeneous and anisotropic such that fractures developing in the intact rock interact with the pre-existing joints [10]. In addition, the presence of weak planes, being sources of large deformation and low shear strength, contributes significantly to the anisotropic behavior of rocks [16, 19, 47].

By contrast to continuum methods, the application of the discrete element method to simulate jointed rock mass has the following advantages: (i) the failure and fracture development caused by a joint face can be simulated free from the limits of the mesh deformation; and (ii) the distribution of actual joint faces can be considered. Thus, the discrete element method (DEM) is a promising approach to capture the heterogeneous and anisotropic nature of rock mass and assess the failure process and the strength of jointed rock masses. Bahaaddini et al. [4, 5] simulated uniaxial compression tests for non-persistent jointed samples and investigated the dependence of different failure modes on the joint dip and overlap angles and joint spacing by analyzing contact force distribution and bond breakage. Yang et al. [73] studied uniaxial compression tests for non-persistent jointed rock samples by analyzing the effects of joint gap, dip angle, and persistency. They concluded that the contact and interaction of joint surfaces have significant effects on the mechanical behavior of jointed rock blocks.

Chen et al. [9] showed that the effect of joint strength mobilization includes not only multi-peak deformation behavior but also strength reduction and increasing deformability features.

In the aforementioned experimental work and the corresponding discrete element modeling, only block-jointed samples and samples with medium or small non-persistent joints were studied. Indeed, very few experiments have been performed for samples under confined compression with multiple sets of large persistent joints, which can be considered as a natural representative of a rock mass characterized by discontinuity, heterogeneity, anisotropy, and non-elasticity.

The objective of this study is to investigate the micro-scale behavior of brittle rock material under confined compressive loading with different joint configurations. A two-dimensional bonded-particle model (BPM) is developed to model the behavior of brittle rock. Model validation is carried out by comparing the numerical results with laboratory tests performed on Blanco Mera (BM) granite material. Joint intensity-related phenomena such as fracture patterns and modes, the shape of the stress–strain curve, and the post-peak strength reduction (degradation) are studied. Detailed analyses are performed to investigate the evolutions of the microstructure of the rock mass for different joint set configurations in terms of the occurrence, propagation, and coalescence of micro-cracks. In addition, several important aspects are also examined including evolution of energy transition, coordination number, fabric and anisotropies of contact normal (a unit vector perpendicular to the direction of contact between two particles) and contact forces, modes of microcracks in terms of shear or tensile failure of parallel bonds.

2 Model description

2.1 The discrete element method (DEM)

The discrete element method, or DEM [12], has been used extensively to model the mechanical behavior of rocks and soils [11, 14, 15, 20–23, 38, 52, 53, 55, 66, 68, 69, 74, 81–83]. In rock mechanics, the bonded-particle model (BPM) [48] allows for the rock to be simulated using a statistically generated assembly of bonded particles at the micro-scale level. The BPM reflects the macro-characteristics by assigning different micro-parameters to particles and bonds to reproduce realistic features and to capture the response of brittle rocks. The smooth-joint contact model in bonded-particle systems provides the DEM model with the ability to simulate fracture propagation within a rock mass with persistent or non-persistent joints under selected loading conditions.

Discrete element modeling of jointed rock masses essentially comprises four components [44, 48, 62]:

1. *Discrete spherical/disk elements*: of a finite radius r , mass density ρ , and a friction coefficient μ . These discrete particles obey Newton's laws of motion and can interact when they are either in contact or bonded.
2. *The force–displacement law*: for the linear parallel-bond model updates the contact force and moment [36]:

$$\mathbf{F}_c = \mathbf{F}^l + \mathbf{F}^d + \bar{\mathbf{F}} \tag{1}$$

$$\mathbf{M}_c = \mathbf{M} \tag{2}$$

where \mathbf{F}^l is the linear elastic force, \mathbf{F}^d is the dashpot force, $\bar{\mathbf{F}}$ is the parallel-bond force, and $\bar{\mathbf{M}}$ is the parallel-bond moment. The parallel-bond force is resolved into a normal and shear force, and the parallel-bond moment is resolved into a twisting and bending moment [36]:

$$\bar{\mathbf{F}} = -\bar{F}_n \hat{\mathbf{n}}_c + \bar{\mathbf{F}}_s \tag{3}$$

$$\bar{\mathbf{M}} = \bar{M}_t \hat{\mathbf{n}}_c + \bar{\mathbf{M}}_b \quad (2D \text{ model} : M_t \equiv 0) \tag{4}$$

where $\hat{\mathbf{n}}_c$ is the unit vector that defines the contact plane. Detailed information regarding the increments of elastic force and moment can be found in Potyondy and Cundall [48].

3. *Parallel Bonds*: In a bonded discrete element system, each element is bonded to its neighboring elements with which it is in contact using springs and linear elastic beams of circular cross section (see Fig. 1a). The maximum tensile and shear stresses acting on the parallel-bond periphery are calculated from the beam theory as [48]:

$$\bar{\sigma} = \frac{\bar{F}_n}{A} + \frac{\|\bar{M}_b\|\bar{R}}{\bar{I}} \tag{5}$$

$$\bar{\tau} = \frac{\|\bar{\mathbf{F}}_s\|}{A} + \begin{cases} \frac{\|\bar{M}_t\|\bar{R}}{J}, & 3D \\ 0, & 2D \end{cases} \tag{6}$$

where $\bar{F}_n, \bar{\mathbf{F}}_s$ are normal and shear parallel-bond force, $\bar{M}_t, \bar{\mathbf{M}}_b$ denote twisting and bending parallel-bond moments;

If the tensile strength limit is exceeded $\bar{\sigma} > \bar{\sigma}_c$, then the bond breaks in tension. If the bond does not break in tension, then the shear strength limit is enforced. The shear strength $\bar{\tau}_c > -\sigma \tan \bar{\phi} + \bar{c}$, where $\sigma = \frac{\bar{F}_n}{A}$ is the average normal stress acting on the parallel-bond cross section. If the shear strength limit is exceeded ($\bar{\tau} > \bar{\tau}_c$), then the bond breaks in shear.

4. *Joints*: With the introduction of the smooth-joint contact model, the bonded-particle DEM model with embedded smooth joints allows for the generation of an

equivalent anisotropic jointed rock mass. After generation of the joint plane, a smooth joint is assigned at the contacts of particles with centers located on the opposite sides of the joint plane. At these contacts, the bonds are removed and smooth joints are defined in a direction parallel to the joint plane (see Fig. 1b). Particles intersected by a smooth joint may overlap and pass through each other rather than be forced to move around one another.

A smooth joint can be envisioned as a set of elastic springs uniformly distributed over a circular cross section, centered at the contact point, and oriented parallel with the joint plane. The area of the smooth-joint cross section is given by [36]:

$$A = \pi R^2 \tag{7}$$

with $R = \lambda \min(R^{(1)}, R^{(2)})$ where $R^{(1)}$ and $R^{(2)}$ are the radii of the two contacting entities (disk/sphere).

The force–displacement law for the smooth-joint model updates the contact force (Fig. 1b) as given by [36]:

$$\mathbf{F}_c = \mathbf{F}, \quad \mathbf{M}_c \equiv 0 \tag{8}$$

where \mathbf{F} is the smooth-joint force. The force is resolved into normal and shear forces:

$$\mathbf{F} = -F_n \hat{\mathbf{n}}_j + \mathbf{F}_s \tag{9}$$

The shear strength is also computed as:

$$F_s^u = -\mu F_n \tag{10}$$

More information related to the computation of the normal and shear forces can be found in Itasca Consulting Group [36].

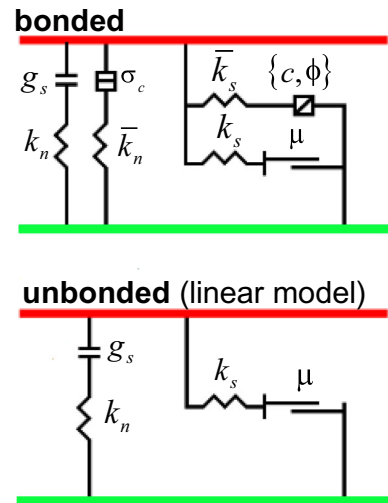
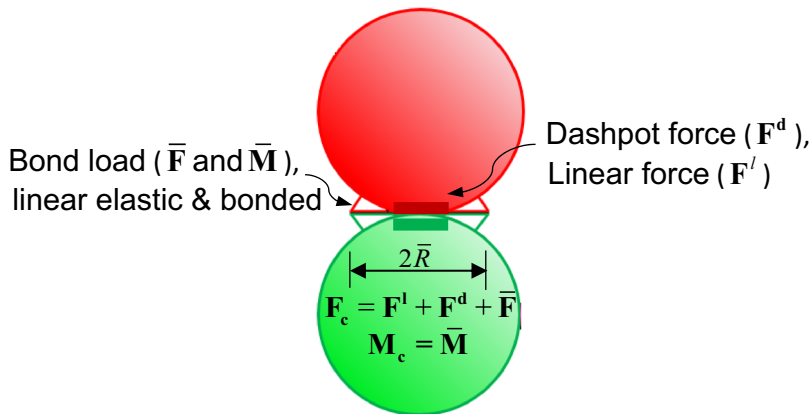
2.2 Model calibration

In DEM, the macro-behavior of the material is derived from the interaction of micro-components where the input properties of these micro-constituents are usually unknown. Therefore, these micro-properties have to be determined through a calibration process [3, 22, 71, 78]. In the calibration process, the appropriate micro-properties are chosen in which the mechanical behavior of the model is directly compared against the measured response of a physical material [36, 48].

2.2.1 Calibration of intact rock models

Laboratory experiments of Alejano et al. [1] on intact rocks were first simulated to calibrate the material parameters of the parallel-bonded model and the contact of particles. This starts with the generation of a dense packing of non-uniform and well-connected grain assembly with a specified

(a) Contact model for the rock



(b) Contact model for the joint set

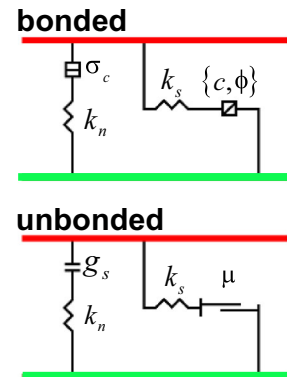
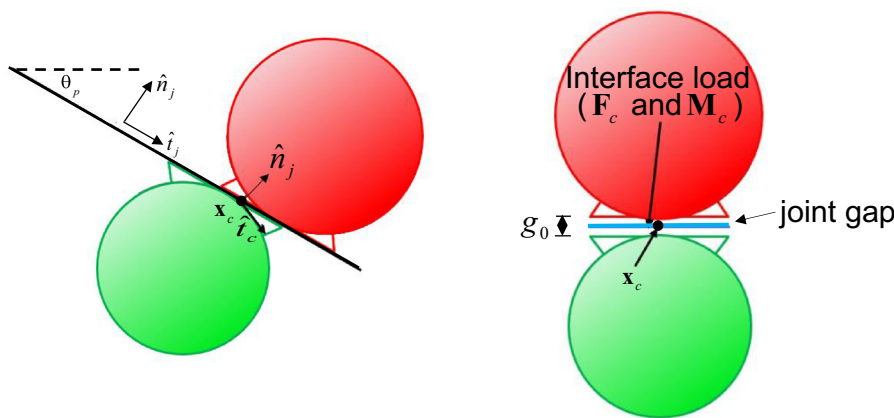


Fig. 1 Behavior and rheological components of **a** the linear parallel-bond model; **b** the smooth-joint model

nonzero material pressure and the installation of parallel bonds at grain–grain contacts. A polyaxial vessel consisting of frictionless walls with a mean width of 54.0 mm and a mean height of 96.7 mm is constructed to match the dimensions of laboratory sample. Subsequently, an assembly of grains with diameters satisfying a uniform size distribution ($R_{\max}/R_{\min} = 1.66$) is generated and then allows them to rearrange into a packed state under conditions of zero friction until static equilibrium is obtained. The material friction coefficient is set to the particles, and a confinement pressure of 4 MPa is applied to be consistent with the experimental conditions. The confinement is applied by moving the vessel walls under control of the servomechanism until the wall pressures are within the specified pressure tolerance of the material pressure and static equilibrium is established. The parallel bonds then

are implemented, and final material properties are assigned to the grain–grain contacts.

However, these material properties cannot be measured directly from laboratory experiments; thus, extensive calibration process is unavoidable, which requires an iterative process to reproduce the mechanical properties of intact rocks at the laboratory scale of Alejano et al. [1]. Particle contact modulus (E_c), particle normal/shear stiffness ratio (\bar{k}_n/\bar{k}_s), parallel-bond modulus (\bar{E}_c), and parallel-bond normal/shear stiffness ratio (\bar{k}_n/\bar{k}_s) are first varied to match the Young's modulus and the Poisson's ratio of the intact rocks. Peak strength is then matched by varying the parallel-bond normal and shear strength. The calibrated values of microscopic parameters are listed in Table 1. The stress–strain behavior of the DEM model compared with that obtained from laboratory test on intact rocks under confining pressure of 4 MPa is illustrated in Fig. 2a. It can be

Table 1 Numerical parameters used in the discrete element analysis

Item	Micromechanical properties
<i>Rock</i>	
Ball–ball contact effective modulus	27.0 GPa
Ball stiffness ratio (k_n/k_s)	2.0
Ball friction coefficient	0.5
Parallel-bond effective modulus	27.0 GPa
Parallel-bond stiffness ratio (\bar{k}_n/\bar{k}_s)	2.0
Parallel-bond tensile strength	148 MPa
Parallel-bond cohesion	148 MPa
<i>Joint set</i>	
Smooth-joint normal stiffness (k_n^{sj})	420 GPa
Smooth-joint shear stiffness (k_s^{sj})	210 GPa
Smooth-joint friction coefficient (μ^{sj})	0.839
Smooth-joint tensile strength (σ_t^{sj})	0 MPa
Smooth-joint cohesion (c^{sj})	0 MPa
Smooth-joint dilation angle (ψ)	0°

seen that the adopted parameters can reasonably simulate the mechanical behaviors of BM granite under confined compression. A comparison of macro-properties of the intact sample by the numerical test and physical test is presented in Table 2.

Table 2 Comparison of target and achieved macro-mechanical parameters of intact and jointed rock samples

	Intact rock sample		Jointed rock sample	
	Experiment	DEM	Experiment	DEM
Deformation modulus (GPa)	28.67	31.74	11.74	14.08
Peak strength (MPa)	185.87	187.06	129.13	131.29

2.2.2 Calibration for rock mass models

After the intact rock behavior simulated by DEM is validated, reliable rock mass models then need to be built that can reflect the mechanical behavior of jointed rock masses with that obtained from laboratory experiments. Therefore, two sets of joint planes, i.e., 1 sub-vertical and 2 sub-horizontal (1V + 2H) jointed samples, are introduced (see Table 3) to match the patterns observed in the laboratory experiments of Alejano et al. [1].

Likewise, there is a need to identify the corresponding micro-properties for the smooth-joint contact model. The SJ model has six essential parameters: joint normal stiffness (k_n^{sj}), shear stiffness (k_s^{sj}), joint tensile strength (σ_t^{sj}), joint cohesion (c^{sj}), joint friction (μ^{sj}), and dilation angle (ψ). Considering that the joint surfaces used in the laboratory experiments are planar and smooth, σ_t^{sj} , c^{sj} and ψ values are all set to 0 in the numerical model.

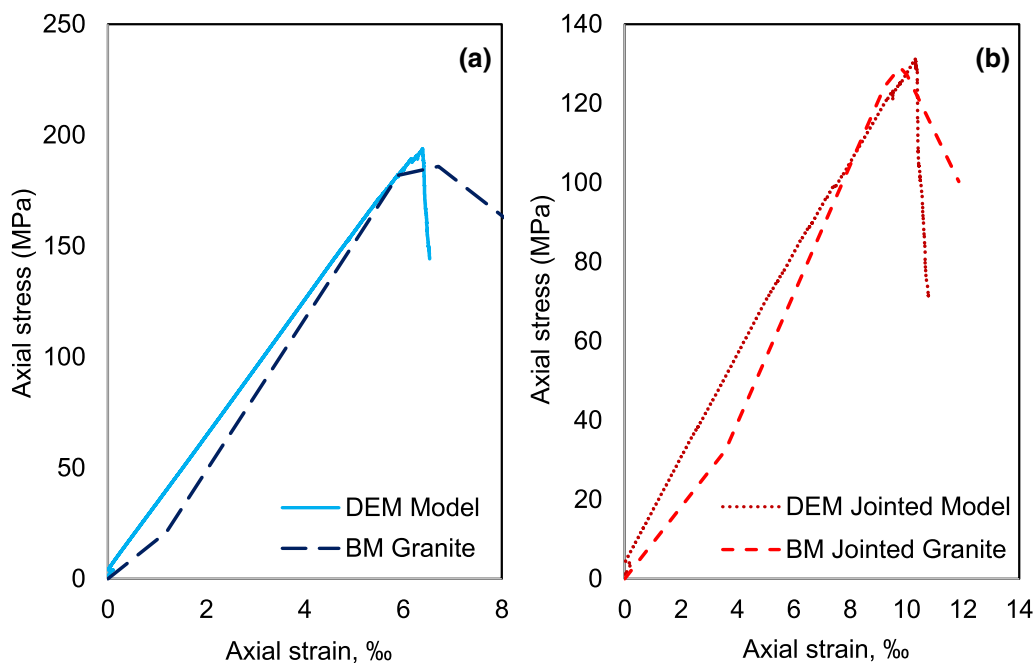
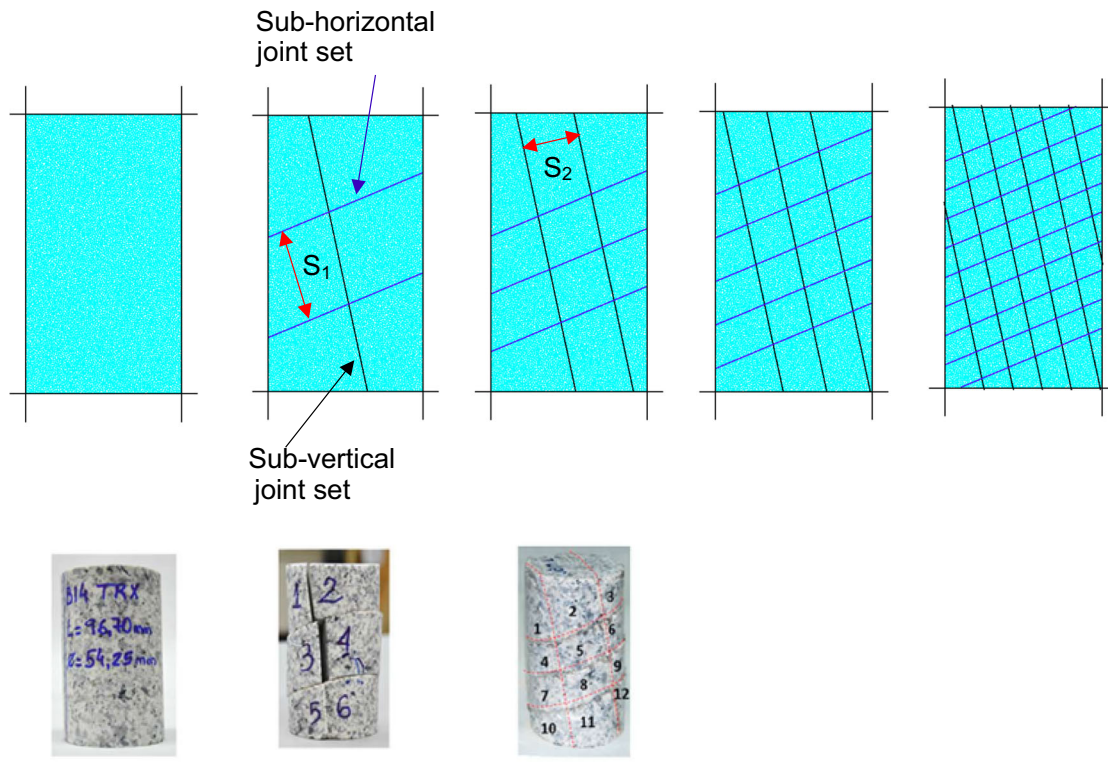


Fig. 2 Stress–strain responses of **a** BS granite and DEM model; **b** BS jointed granite and DEM jointed model for validation micro-parameters

Table 3 Numerical configurations of rock blocks

Intact	1V + 2H $S_1 = 35$ cm	2V + 3H $S_1 = 20$ cm $S_2 = 20$ cm	3V + 5H $S_1 = 15$ cm $S_2 = 15$ cm	6V + 9H $S_1 = 10$ cm $S_2 = 10$ cm
--------	--------------------------	---	---	---



Experimental figures are obtained from Alejano et al. [1]

The strength and deformation modulus of a jointed rock depend on joint stiffness and frictional resistance. In the calibration process, k_n^{sj} is first determined using the inverse calibration method. This means that the joint normal stiffness k_n^{sj} is adjusted until the target value of the deformation modulus E_m measured in the laboratory experiment is reached. It is noted that the deformation modulus is calculated from the slope of stress–strain curves at 50% of the peak stress. The ratio of k_n^{sj}/k_s^{sj} is then set to 2 as suggested by Vergara et al. [61]. Finally, μ^{sj} is adjusted to achieve the desired peak strength, which is consistent with the friction angle reported in the literature for similar granite samples [31].

Figure 2b compares the numerical and experimental results, showing that the macro-response captured by the

numerical model for the 1V + 2H jointed samples is in agreement with the experimental results. Quantitatively, the achieved macro-mechanical properties obtained numerically are reasonably close to the experimental results (see Table 2). Thus, the derived joint stiffness values and joint friction that reproduce deformation modulus and the strength of are the calibrated micro-properties of the joints (listed in Table 1). However, compared to the calculated linear elastic deformations, the experimental stress–strain curves of the both intact and jointed samples at low stress levels (Fig. 2) show concave (hardening) and nonlinearity, which mainly result from the closure of the pre-existing fissures or cracks in natural rock at the initial loading stage [44].

Since the main objective of this study is to investigate the influence of increased density of initial jointing on the macroscopic behavior and the underlying micromechanical mechanism, it is not required to fully reproduce all the responses under different confining pressures. The performance of the numerical models subjected to confining pressure of 4 MPa is, therefore, evaluated and found to agree well with the experimental results.

2.2.3 Rock mass configuration for the numerical analysis

Once the discrete element models are validated, the mechanical behavior of the jointed rock masses with various configurations of joint sets can be investigated. Besides, the aforementioned intact and 1V + 2H jointed samples, three models representing 2V + 3H, 3V + 5H, and 6V + 9H jointed samples were developed. Additional data can then be generated to supplement laboratory tests, which compensates for the shortcomings of laboratory experiments. This numerical study has the merits of investigating the influence of the level of initial jointing on the macroscopic characteristics of the fracturing process of rock masses and the underlying mechanisms at the microscopic level. A detailed description of the jointed rock configuration is given in Table 3.

3 Numerical results and discussion

With the verified mechanical parameters, a discrete element numerical confined compression tests on both intact and jointed granite samples can be performed to investigate the deformability and failure mechanism thoroughly from micro–macro-behavior, including stress–strain relation, failure modes, kinematic activities, energy budgets, fabric evolutions, contact force distributions, and microstructure anisotropies.

3.1 Deformation and failure processes

3.1.1 Mechanical response

The stress–strain relationships as well as the number of micro-cracks generated for the intact and jointed rocks models in triaxial compression with 4.0 MPa confining pressures are presented in Fig. 3. The following observations can be made from this figure:

1. Pre-existing discontinuities have significant effects on the stiffness, peak strength, and axial strain at peak. For example, a significant decrease of stiffness and peak strength is found with the increase of initial joint frequency, and the corresponding information is presented in Table 4.
2. The onset of microcracking, also associated with material yielding, occurs at approximately 50–55% of the peak stress in agreement with the experimental observations of Alejano et al. [1]. In addition, with the increase in the joint density, strain hardening becomes more apparent as reflected by the deviation of the stress–strain curve with respect to its initial slope. This is because the increasing dominance of joint slip yielding mechanism in the increasingly jointed rock samples contributes to strain hardening, which is also in line with the conclusion made by Walton et al. [64].
3. The transition from brittle behavior, at zero or low level of initial jointing, to more ductile behavior, at high intensity of pre-existing discontinuity, can be clearly observed in the stress–strain responses of intact (Fig. 3a) and 6V + 9H samples (Fig. 3e), respectively. The increase in ductility with the increase in the degree of initial jointing is attributed to the highly jointed structure that largely suppresses the localization and coalescence of microcracks. This in turn inhibits the formation of a throughgoing macro-rupture plane associated with catastrophic failure. Consequently, the increase in initial joint frequency leads to reduced number of cracks with no apparent coalescence and more ductile response.
4. With the increase in the degree of initial jointing, the evolution of cumulative micro-cracks transits from a surge with rapid increment of cracks into a step-wise manner characterized by an accumulation of cracks at a relatively slower rate. This is mainly due to the fact that the addition of further joints to the sample interrupts the localization and coalescence of freshly formed cracks, with a higher tendency for the rock mass to disaggregate along the joint planes.
5. The number of shear cracks decreases significantly with increased density of initial joints, especially for the 6V + 9H samples, where no shear crack is generated during the entire deformation and failure process. This can be attributed to the fact that the cohesive rock unit is split into jointed blocks along the fully persistent joint sets. Microcracks are generated during the sliding of the jointed blocks at the emergent asperities along the pre-existing joints. Thus, the growth of fractures in the 6V + 9H rock samples occurs through the plucking of particles along the pre-existing joints as a result of the sliding of the jointed blocks, which is predominantly generated in tensile mode.

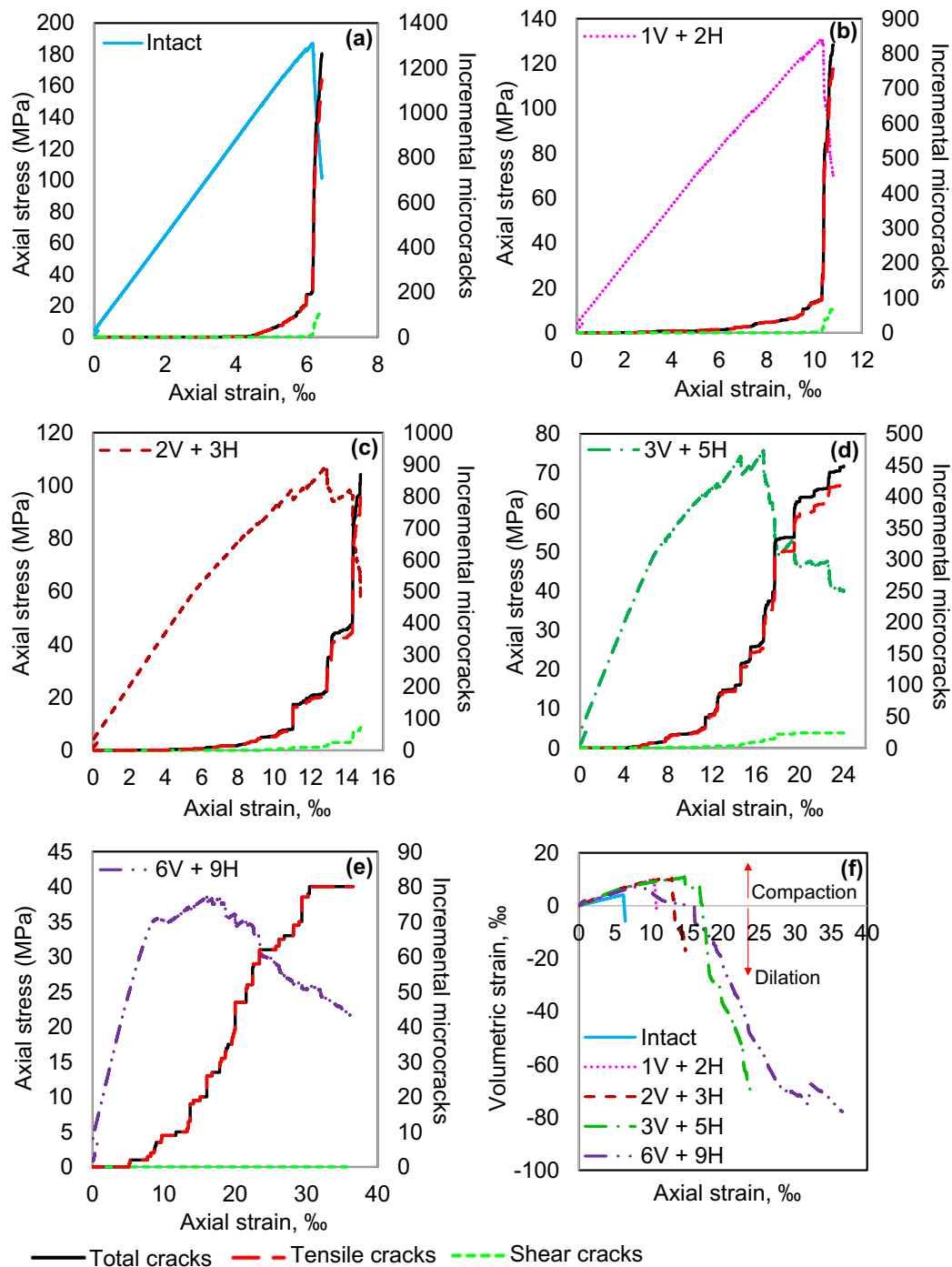


Fig. 3 Stress–strain responses of **a** intact **b** 1V + 2H, **c** 2V + 3H, **d** 3V + 5H and **e** 6V + 9H rock samples; **f** volumetric strain versus axial strain in numerical confined compression experiments

3.1.2 Failure mode and orientations of microscopic cracks

Each jointed block consists of intact portions of the model material interspaced with joints [35]. The effects of persistent rock discontinuities on the failure pattern of rock masses were reported in Kulatilake et al. [34, 35], Singh et al. [58], Wang and Huang [67], Xu et al. [72], Shang et al. [54]. Three

primary modes of rock mass failure are reported, namely failure through intact material, sliding on the joint plane, and mixed failure of the above two modes. Moreover, it is worth noting that microcracking has two modes, i.e., tensile and shear microcracks. A tensile microcrack forms when inter-particle normal stress exceeds the tensile strength of the bond. Similarly, a shear microcrack results when local shear

Table 4 Strength and deformability of intact and increasingly jointed samples

	Intact	1V + 2H	2V + 3H	3V + 5H	6V + 9H
Peak strength (MPa)	187.06	131.29	107.35	75.74	38.58
Deformation modulus (GPa)	31.74	14.08	10.91	7.69	5.32

stress exceeds the shear strength of the bond in compression. To better investigate the influence of pre-existing discontinuities on the failure mechanisms of rock masses, detailed observations of various failure modes based on the damage behavior, orientations of microscopic cracks, and fragmentation characteristics are analyzed and discussed below.

Intact rock failure: the main mechanism of failure is the development of the macro-shear plane within the intact rock samples, and the formation of axial splitting zone or tensile failure within the intact rock blocks for the jointed 1V + 2H rock sample (Fig. 4a). The models exhibit high compressive strengths and brittle behavior [34]. No macroscopic movements parallel or normal to the planes of the pre-existing discontinuities are observed. Failure occurs through the intact material exhibited by the sequence of elastic deformation, crack initiation, propagation, and crack coalescence. Consequently, large amount of fractures can nucleate and grow to completion, thus resulting in the disintegration of solids (i.e., the intact rock or jointed rock blocks) into smaller pieces. These pieces (i.e., fragments) are identified as sets of particles connected by the surviving bonded contacts as a consequence of the fragmentation process. Both tensile and shear cracks tend to nucleate in specific areas in the samples and form organized patterns, which are correlated with areas of high fragmentation concentration. The formation of well-organized cross-like shear band results from the coalescence of both tensile and shear cracks which clearly defines the contour of the sheared zone as shown in Figs. 4a and 6.

For intact rock, it can be observed that the orientation of microscopic tensile cracks is predominantly parallel to the direction of the maximum principal stress [13]. This is attributed to the dilation of the sample in the direction perpendicular to the loading (Poisson’s effect). For the jointed 1V + 2H samples, the orientation of shear microcracks exhibits more isotropic. On the other hand, the concentration of tensile microcracks is found to deviate towards the direction of the sub-vertical joints with a mean dip of 77.9° in the jointed 1V + 2H samples.

Sliding along joint plane: for jointed 6V + 9H rock samples, the main mechanism of failure is sliding along the pre-existing discontinuities and thus the behavior of joints plays a

dominant role on the global deformation, which are characterized by a dramatic decrease in the number of micro-tensile cracks and the absence of micro-shear cracks. This failure mode is associated with large deformations and subsequent dilations of the sample in the minor principal stress direction (see Fig. 4a). These samples exhibit a significant ductile behavior characterized by a relatively low peak strength at greater axial strain and slower drop in post-peak strength. Only a small number of fragments are squeezed out due to the movement of the rock block (see Fig. 4b).

Mixed failure: the predominant failure mechanism for 2V + 3H and 3V + 5H rock samples is partly through intact rock failure and partly through pre-existing discontinuities. The orientation distribution of shear cracks transforms from distributed to predominantly vertical. The failure mode observed involves failure through the intact rock, which is also controlled by the interaction with pre-existing joints and the interlocking of the model blocks, inducing a gradual spreading of internal damage and relative movement of blocks along pre-existing joints. Thus, the rock mass can either disaggregate along the pre-existing discontinuities or break along freshly formed faces resulting in fragments being generated at block corners. This phenomenon is consistent with the experimental observations in Alejano et al. [1], and the numerical modeling of the failure mode of jointed rock blocks reported by Huang et al. [31] and Zhou et al. [84].

3.1.3 Particle-level kinematics and contact force information

The influence of rock discontinuities on the mechanism of rock failure can be captured through the distributions of particle-level kinematics, such as the translational and rotational granular temperatures, local strain, and void ratio, which are excellent indicators of damage evolution.

Granular temperature is proportional to the average value of the square of the grains’ velocity fluctuations, with respect to their mean velocity. It can be used to quantify particle-level kinematical activities [41, 42]:

$$v_x'' = v_x^i - \overline{v_x^i} \tag{11}$$

$$v_y'' = v_y^i - \overline{v_y^i} \tag{12}$$

$$\omega'' = \omega^i - \overline{\omega^i} \tag{13}$$

where translational velocity components v_x^i , v_y^i and angular velocity component ω^i of the selected i -th particle in the selected spherical region Ω_i can be divided into the mean velocity components $\overline{v_x^i}$, $\overline{v_y^i}$, and $\overline{\omega^i}$ and fluctuating parts v_x'' , v_y'' , and ω'' .

The mean velocity components, $\overline{v_x^i}$, $\overline{v_y^i}$, and $\overline{\omega^i}$ can be attained by averaging the velocities of particles

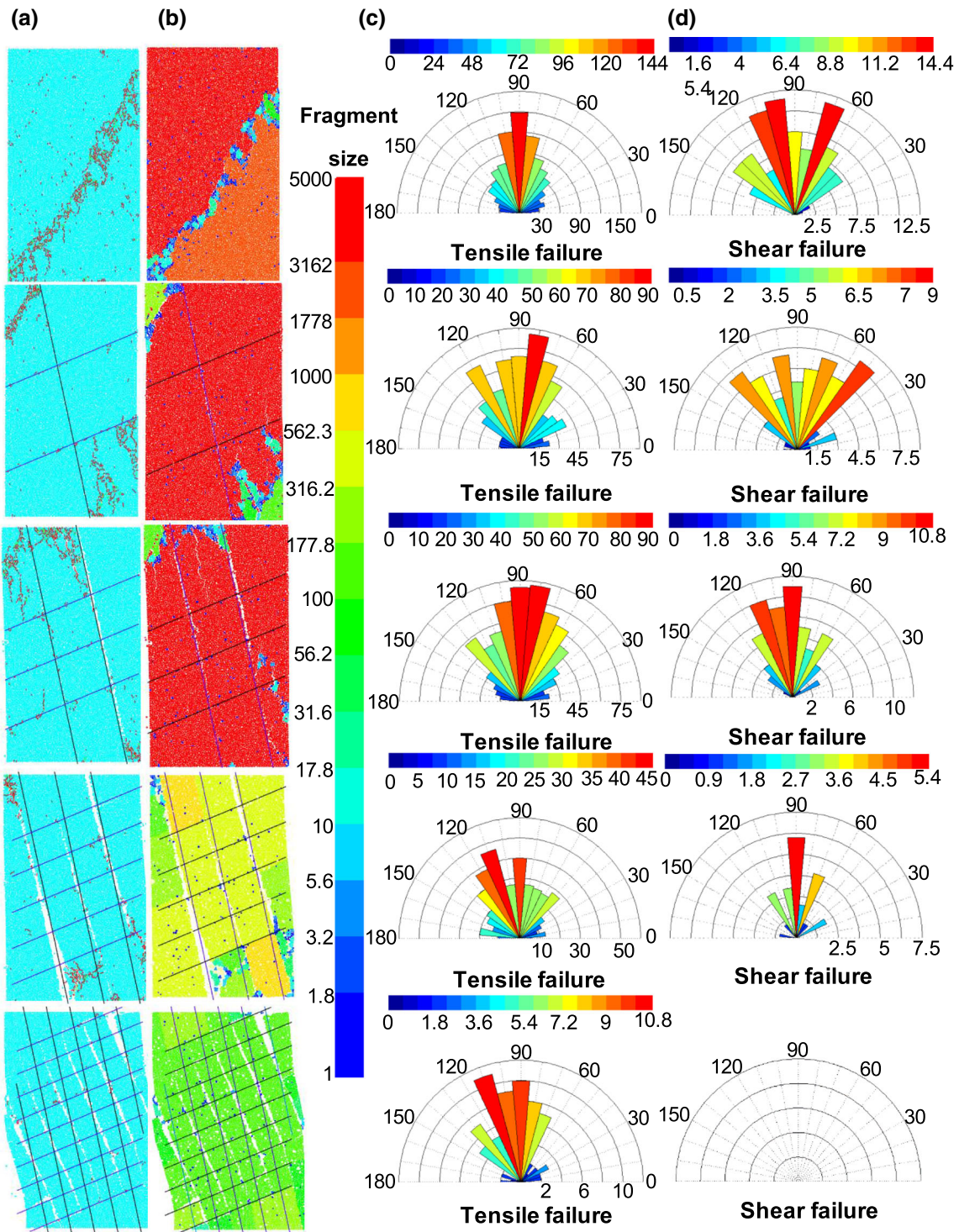


Fig. 4 **a** Micro-crack distribution within the rock mass samples; **b** fragment size distributions presented by the logarithmic hue scale; **c** polar histogram for tensile failure; **d** polar histogram for shear failure at the final damage stage

surrounding the selected i -th particle in the chosen spherical region Ω_i [41, 42]:

$$\overline{v_x^i} = \frac{1}{n} \sum_{j=1}^n v_x^j \quad (14)$$

$$\overline{v_y^i} = \frac{1}{n} \sum_{j=1}^n v_y^j \quad (15)$$

$$\overline{\omega^i} = \frac{1}{n} \sum_{j=1}^n \omega^j \quad (16)$$

$$(x_j - x_i)^2 + (y_j - y_i)^2 \leq r^2 \quad (17)$$

where r is the radius of the spherical region Ω_i . In this study, the neighborhood size is set to $4d_{\max}$ (see Fig. 5a).

Hence, the translational T_V^i and rotational T_R^i granular temperatures representing the intensity of particle exchange (analogous to a thermodynamic temperature) are calculated from the velocity fluctuations as expressed below [41, 42]:

$$T_V^i = \frac{1}{2} [(v_x^i)'^2 + (v_y^i)'^2] \quad (18)$$

$$T_R^i = \frac{I}{2m} (\omega^i)'^2 \quad (19)$$

where I and m are moment of inertia tensor and mass of the particle.

Following Wang et al. [65] and Ma et al. [41], a mesh-free strain calculation method is adopted in this study. The mesh-free method used in this study employs a grid-type discretization over the reference configuration. A grid spacing of the median particle diameter (d_{50}) is suggested to capture the shear localization at a satisfactory resolution. A rectangular grid is superimposed over the volume of particles prior to any deformation and serves as the continuum reference space (see Fig. 5b). Each grid point in the reference space is, then, assigned to an individual particle j such that [65]:

$$\frac{d_j}{r_j} \leq \frac{d_i}{r_i} \quad (i = 1, 2, \dots, N_p; i \neq j) \quad (20)$$

where r_i is the radius of particle i , d_i is the distance between the centroid of particle i and the considered grid node, and N_p is the number of particles. If the distance ratio between particle centroid and its associated grid node to the particle radius is the smallest among all particles, then the association from this particle to the considered node is constructed [65].

The displacement of the grid point is calculated by [65]:

$$u_x^g = u_x^p + d[\cos(\theta_0 + \omega) - \cos \theta_0] \quad (21)$$

$$u_y^g = u_y^p + d[\sin(\theta_0 + \omega) - \sin \theta_0] \quad (22)$$

where u_x^g, u_y^g and u_x^p, u_y^p are the x and y are displacement components of the grid point and particle centroid, respectively; d is the distance between the grid point and the particle centroid; θ_0 is the initial phase angle of the grid point location relative to the particle centroid; and ω is the accumulated rotation of the particle (Fig. 5c).

On account of the particle rotation, this method is able to capture accurately the actual strains that the granular media are experiencing. Therefore, the Green–St Venant strain tensor E_{ij} can be obtained at any stage of the simulation [65]:

$$E_{ij} = \frac{1}{2} (u_{i,j} + u_{j,i} + u_{k,i}u_{k,j}) \quad (23)$$

where $u_{i,j}$ is the displacement gradient tensor over the grid, which is based on the deformation measure related to the reference configuration.

It is found, in Fig. 6, that a strong degree of spatial association exists among the localization patterns of the kinematic quantities, shear strain, void ratio, contact force chains at the final damage stage (50% post-peak stress state), indicating their consistency in depicting the failure mechanism of the intact/pre-jointed rock models. Distinct localization bands can be observed in intact rock, where the localized shear strains and high void ratios in the granular assemblage are accompanied with high granular temperatures and strong

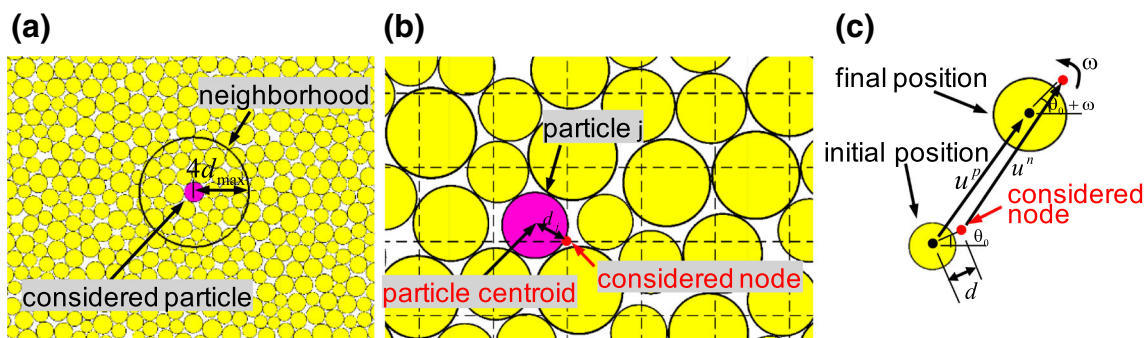


Fig. 5 Schematic illustrations of **a** definition of the neighborhood of a particle; **b** association of grid node to particle, and **c** displacement of grid node and its associated particle

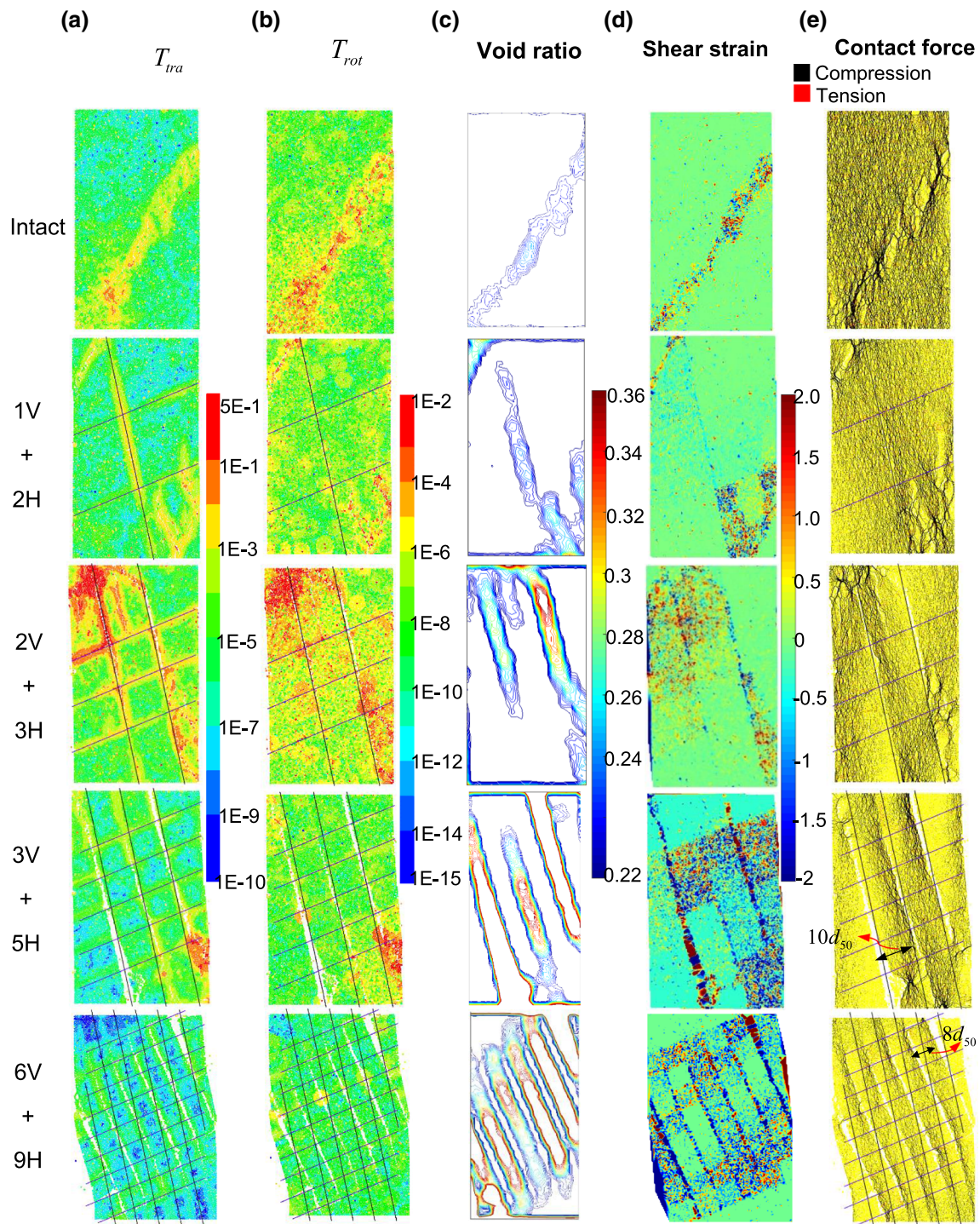


Fig. 6 **a** distribution of translational granular temperature, T_{tra}^i ; **b** distribution of rotational granular temperature, T_{rot}^i ; **c** contour of void ratio; **d** contour of localized shear strains; **e** contact force chain at the final damage stage

force chain confined within a thin zone along the rupture surface, as shown in Fig. 6. Within this zone of primary shear fracture, the high granular temperature distributions (that indicate rapid particle exchange and higher rates of particle collisions) are mainly caused by the significant amount of bond breakage. The nucleation and coalescence of fractures

result in a loss of interparticle bonds and a reduction in rock strength, imparting permanent changes in solid structure. Therefore, a growing number of particles are more susceptible to movement and change positions more intensely with nearest neighbors, implying more pronounced higher granular temperatures.

In contrast to intact rock samples, no visible bands of particles with high temperature are found in the 6V + 9H samples, which indicates that the localized shear bands are not formed in the bonded granular assembly (see Fig. 6). This is generally interpreted as a dominance of frictional sliding along the joint planes with a low percentage of interparticle bond breakages instead of localization of large amounts of fractures. Comparing to the intact rock failure mode, the difference is that the particles of the 6V + 9H samples remain largely bonded and move as rigid blocks while experiencing significant frictional movement. A few microcracks involved in the failure mode of sliding along pre-existing joints result from the breakage of particle conglomerates (or “coarse fragments”) resisted by the frictional sliding process.

It is worth noting lack of distinct shear band is found in jointed samples. Instead, irregular, local zones of strain localization are observed in 1V + 2H, 2V + 3H, and 3V + 5H samples where intense fracturing activities are evidenced by the heterogeneous distribution of granular temperatures and localized distribution of contact force chains and void ratios. This phenomenon is expected as the breakage of bonds contributes to the nucleation and growth of fractures leading to the interparticle locking being reduced; thus, fractured blocks are capable of moving and rotating freely manifesting the enhanced granular temperatures.

Compared to that of 1V + 2H samples, more intense granular agitations with frequent collisions depicted by the translational and rotational granular temperatures are observed for 2V + 3H and 3V + 5H rock samples where the mixed failure mode dominates the deformation and damage process. It suggests that additional degrees of freedom for interparticle motion are created not only by fracturing of the intact rock material but also the interaction with pre-existing discontinuities.

3.1.4 Spatial correlation and contact force heterogeneity

A more quantitative characterization of the influence of the initial joint density level on force chain structure can be obtained by computing the 2D spatial correlation function $G(r)$ of the magnitude of the normal contact forces acting on the particles. The $G(r)$ is defined in the same manner as in Løvoll et al. [40]:

$$G(r) = \frac{\sum_{i=1}^N \sum_{j>i} \delta(|r_{ij} - r|) f_i f_j}{\sum_{i=1}^N \sum_{j>i} \delta(|r_{ij} - r|)} \quad (24)$$

where N is the total number of contact points, f_i is the normalized normal contact force acting at contact i , r_{ij} is

the distance between contacts i and j , and $\delta(0) = 1$. A force pair is two normal forces f_i and f_j separated by r_{ij} which together contribute to the spatial correlation function. A nonzero value of $G(r)$ infers that, on average, two contacts separated by a distance r have forces that are correlated [39, 42]

The correlation demonstrates that two particles at distance r are connected through a cluster of simultaneously contacting particles, and the force from one particle is being transmitted through the network to the other particle [39]. It thereby establishes a quantitative measurement of the average effect of force chains of length r in the assembly. Figure 7a illustrates the correlations of normal contact force for increasingly jointed rock samples at the final damage stage. Note that the radial distance has been normalized with respect to the mean particle diameter d_{50} .

For this 2D discrete element analysis, the minimum separation distance $r_{\min} \approx d_{50}/2$, which is consistent with the numerical observation of Silbert et al. [57]. Obviously, all samples have the strongest peak near $r \approx d_{50}$, and other prominent peaks are found at separation distances of $r \approx 2d_{50}, 3d_{50}$ and $4 d_{50}$. These peaks are all located around integral multiples of the average grain size d_{50} . This corresponds to situations where contact forces are transmitted through the “force chain networks” that propagate from one grain to the next across grain–grain contacts.

Clearly, with the increase in initial joint frequency, the $G(r)$ has higher peaks before r reaches $5d_{50}$, representative of the higher interparticle locking. In addition, the local correlations between the positions of the contact points are stronger in highly jointed samples at the final damage stage, indicating a more tightly connected distribution of contact points in the system as a result of the fewer amounts of microcracking being generated.

The amplitude of oscillation is found to decrease with the increase in radial distance. After extending to a distance greater than five times the mean particle diameters ($5d_{50}$), slight oscillations around unity are observed for intact, 1V + 2H, and 2V + 3H rock samples. However, for jointed 3V + 5H and 6V + 9H rock samples there is an obvious decline in $G(r)$, and this trend continues until r reaches $8d_{50}$ and $10d_{50}$, respectively, for these two samples. This is attributed to the slippage along the joint planes, creating space for each fracture opening with a separate distance being equivalent to $8d_{50}$ and $10d_{50}$, as shown in Fig. 6e.

The above demonstrates a continuous decreasing correlation pattern until fracture opening occurs, which constrains the transmission of contact forces through “force chain networks” formed by the topology of the contact network [39]. It is noted that the $G(r)$ in 6V + 9H jointed samples finally decreases to a value smaller than that of the intact, 1V + 2H, and 2V + 3H rock samples, which

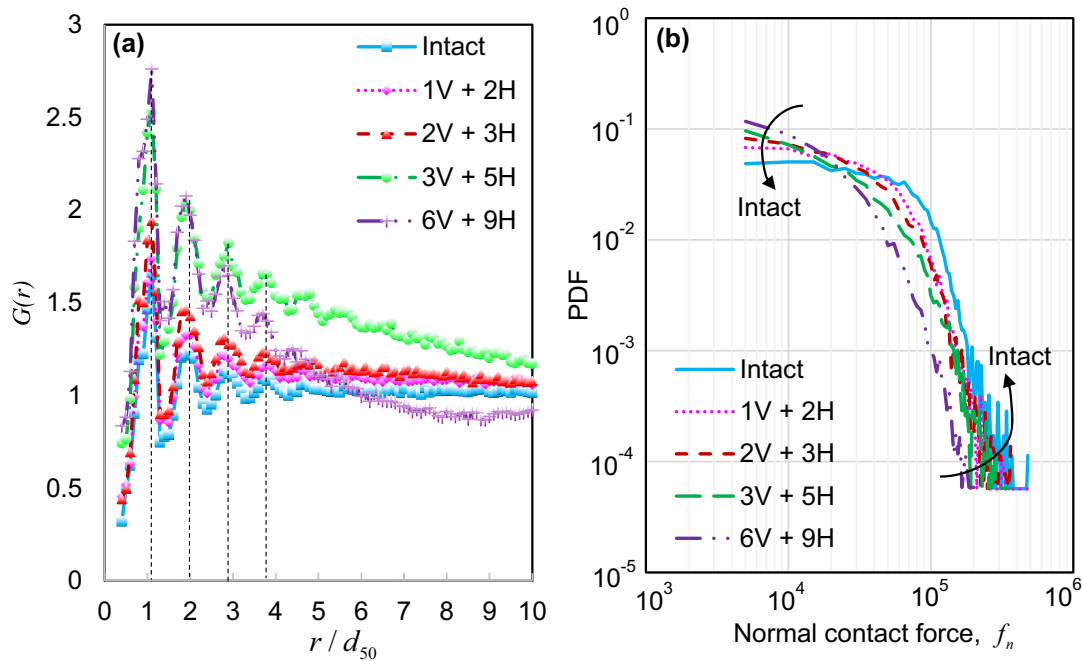


Fig. 7 **a** Spatial force correlation function $G(r)$ for normal contact force plotted as a function of distance r normalized by mean particle diameter d_{50} for intact and jointed samples; **b** probability distributions of normal contact forces f_n in log–log scales for intact and jointed samples

differs from 3V + 5H rock sample that it is still larger than the other three cases. It mirrors the visual prominence of the force chain network in jointed 6V + 9H samples that has much larger fracture openings shown in Fig. 6e. In all cases, the results of this study demonstrate that contact forces are spatially correlated, but are much more affected by the level of initial jointing.

The influence of the level of initial jointing on the contact network can also be illustrated using the probability distribution function (PDF) of contact forces. Clearly, the results shown in Fig. 7b for the PDF of the normal contact forces at post-peak stress state demonstrate that the degree of initial jointing largely affects the contact force distribution. Note that the probability distribution of the tangential contact forces demonstrates a similar trend during compression, so there is no need to repeat it herein. Clearly, the PDF distribution for normal contact forces becomes narrower, and the corresponding inhomogeneity of the stress transmission becomes larger with increasingly jointed rock structure. This decreasing force homogeneity is in the sense that with the increase in initial jointing, the granular media involve less strong force chains in number (see Fig. 6e) as well as the decrease in the magnitude of normal force.

The above can be further corroborated by examining the *Gini* coefficient for the normal force magnitudes. The *Gini* coefficient, often used to represent a nation’s income inequality, describes the homogeneity of some quantity in a population. A *Gini* coefficient of 1 indicates complete inequality, whereas a value of 0 indicates perfect equality

and homogeneity. The definition is the same as that in Hurley et al. [32] and calculated as follows:

$$G = \frac{1}{N_c} \left(N_c + 1 - 2 \left(\frac{\sum_{i=1}^{N_c} (N_c + 1 - i) f_i^n}{\sum_{i=1}^{N_c} f_i^n} \right) \right) \quad (25)$$

The term N_c is denoted as the number of contacts. The increase in *Gini* coefficient indicates more evident inhomogeneity among the whole contact system. The normal contact force f_i^n is sorted in a non-decreasing order ($f_i^n \leq f_{i+1}^n$).

Table 5 indicates that the force heterogeneity intensifies as the initial joint frequency increases, which accords well with the observations from the PDF of the normal contact force.

These two descriptions provide complementary points of view of the microstructure and demonstrate that the increasing heterogeneity of contact force distribution with the increase in the degree of initial joint frequency can be attributed to the increasing number of debonded particles along the joint plane.

Table 5 *Gini* coefficient

	Intact	1V + 2H	2V + 3H	3V + 5H	6V + 9H
<i>Gini</i> coefficient	0.5955	0.6549	0.7098	0.8032	0.8377

3.1.5 Energy budget during deformation

Analyses of the energy budgets are of critical importance to establishing the linkage between micro- and macro-mechanical responses for a comprehensive understanding of the deformation process and failure mechanism of intact and pre-jointed rock. Relevant energy terms include boundary work dE_w , body work dE_b done by gravity force, elastic strain energy dE_s stored at particle contacts, bond energy dE_{pb} stored in parallel bonds, kinetic energy dE_k , frictional dissipation dE_f , damping dissipation dE_d , and the fracture energy E_{frac} , are calculated as the cumulative energy released by all bond breakage in the tensile and shear fracture modes. In this study, the body work dE_b is equal to zero as the gravity acceleration was set to zero.

The energy input due to the walls is represented by [36]

$$E_w^j = E_w^{j-1} + \sum_{i=1}^N F_w \Delta U_w \quad (26)$$

where E_w^j and E_w^{j-1} are the total accumulated work done by all walls on the assembly at the current and previous time steps; F_w is the resultant force acting on the wall; ΔU_w is the applied displacement occurring during the current time step.

According to the first law of thermodynamics, the energy components satisfy

$$dE_w = dE_s + dE_{pb} + dE_k + dE_f + dE_d + dE_{frac} \quad (27)$$

where the last three terms define the plastic energy dissipation dE_p .

For 6V + 9H rock samples (see Fig. 8e), friction dissipation prevails over the strain energy build-up from the very beginning due to lower average coordination number; this situation further demonstrates sliding through the joint plane plays a dominant role in the rock deformation process. In contrast, for intact rocks (Fig. 8a), strain energies are predominantly accumulated due to the elastic compressions at the particle contacts before the occurrence of microcracking marking the onset of inelastic dissipation. The transition in energy evolution is expected as the solid microstructure being more disintegrated with lower contact intensity due to the increased jointing. The energy absorbed by the rock samples stored not only as elastic strain energy but accompanied by plastic energy dissipation due to a large amount of frictional movements occurring along the pre-existing discontinuities.

The major effect of microcracking activity, which itself only dissipates a small amount of the external work, is to promote the changes in solid microstructure by creating additional degrees of freedom for frictional sliding both through pre-existing discontinuities and frictional inter-particle movements. The threshold of strain energy for

initiating the bond breakage decreases with the increase in initial joint frequency, as evidenced by the downward shifts of the trend in Fig. 8. For intact (Fig. 8a) and 1V + 2H samples (Fig. 8b), stress drop occurs rapidly after the peak strength, and the stored energy is released quickly. Elastic and plastic energy does not dissipate gradually in this case. Elastic strain energy significantly reduced, while dissipated strain energy instantly increased to reach the total strain energy value.

The relative contribution of elastic energies to the energy budget declines with the increase in initial joint frequency, accounting for 41.9% of the input energy for intact samples, 20.9% for 1V + 2H samples, 14.8% for 2V + 3H samples, 11.1% for 3V + 5H samples, and 9.1% of the input energy for 6V + 9H samples as illustrated in Fig. 8f. Simultaneously, fracture energy decreases from 279.9 J for the intact sample, 194.2 J at 1V + 2H samples, 190.3 J at 2V + 3H samples, 89.0 J at 3V + 5H samples to 10.9 J at 6V + 9H samples. The tensile and shear components of fracture energies in each case are summarized in Table 6. In addition, it is worth noting that although only 9.1%, 8.4%, 8.3%, and 5.3% of the total microcracks for intact, 1V + 2H, 2V + 3H, and 3V + 5H rock samples, respectively, occur in shear mode, they contribute to 23.3%, 20.8%, 22.1%, and 17% of the fracture energy released for the corresponding rock samples.

It can be observed that fracture energy accounts for a small percentage of the input energy, similar to the energy budget estimations reported by Vora and Morgan [63] for Berea Sandstone and Lac du Bonnet Granite. The decrease in fracture energy with the degree of initial joint frequency is due to the decrease in the number of microcracking activities. Thus, fracture energy is strongly influenced by the modes of microcracks, which is in turn controlled by the rock strength and level of joint intensity.

3.2 Micro-mechanism and macro-response

3.2.1 Evolution of fabric and coordination number

The microstructure, or fabric, of a granular material can be interpreted by the orientation of the contact normal characterizing microscopic features. Satake [51] quantified the fabric using a second-order tensor. In tensorial notation, the second-order fabric tensor (Φ_{ij}) is given as:

$$\Phi_{ij} = \frac{1}{N_c} \sum_{N_c} n_i n_j \quad (28)$$

where N_c is the total number of contacts, n is the unit normal vector of contact with $i, j = 1, 2$ for two-dimensional (2D) analyses.

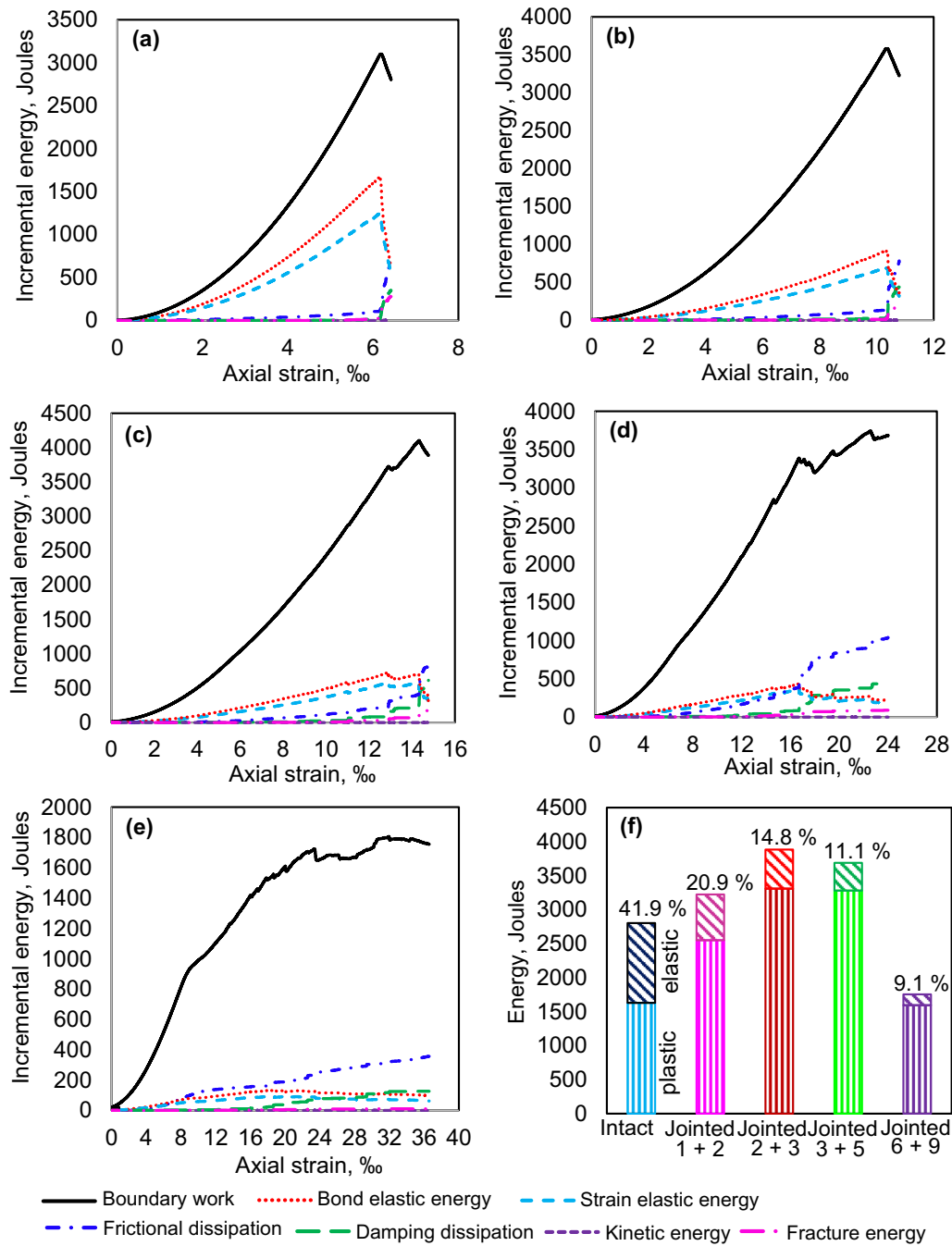


Fig. 8 Evolution of energy in **a** intact, **b** 1V + 2H, **c** 2V + 3H, **d** 3V + 5H and **e** 6V + 9H rock samples; **f** energy partitioning into elastic energy and plastic energy during numerical confined compression experiment

The contact normal is defined as vectors that are perpendicular to the plane defining the contact between two particles. The summation and averaging are taken over all N_c contacts in the contact network.

For 2D analyses, Eq. (28) gives a two-dimensional matrix:

$$\begin{pmatrix} \Phi_{xx} & \Phi_{xy} \\ \Phi_{yx} & \Phi_{yy} \end{pmatrix} = \frac{1}{N_c} \begin{pmatrix} \sum_{N_c} n_x n_x & \sum_{N_c} n_x n_y \\ \sum_{N_c} n_y n_x & \sum_{N_c} n_y n_y \end{pmatrix} \quad (29)$$

The eigenvalues of the fabric tensor give the principal fabrics Φ_1 and Φ_2 , which can be used to describe the intensity of the anisotropy. The degree of anisotropy can be characterized by the deviatoric fabric expressed by [56]:

Table 6 Tensile and shear fracture energy

	Intact	1V + 2H	2V + 3H	3V + 5H	6V + 9H
Tensile fracture energy (J)	214.7	153.9	148.2	73.9	10.9
Shear fracture energy (J)	65.2	40.3	42.1	15.1	0

$$\Phi_1 - \Phi_2 = 2\sqrt{\left(\frac{\Phi_{xx} - \Phi_{yy}}{2}\right)^2 + \Phi_{xy}^2} \quad (30)$$

Four groups of contact normal are analyzed in this study: (i) considering all engaged contacts, (ii) contacts only transmitting compressive force, (iii) contacts only transmitting tensile contacts, (iv) bonded contacts. The corresponding evolutions of the deviatoric fabric of contact normal as a function of the axial strain are illustrated in Fig. 9.

Different patterns of evolutions can be noted for the fabric deviator of all contacts due to the presence of rock discontinuities (see Fig. 9a). For intact rock, deviatoric fabric rapidly increases to a peak value within a small axial strain, whereas deviatoric fabric for 1V + 2H and 2V + 3H samples exhibits a similar upward trend but with significantly smaller peaks. In contrast, deviatoric fabrics for 3V + 5H and 6V + 9H samples act distinctly different where they fluctuate to peak and then evolve to be almost flat. This can be attributed to the fact that the frictional sliding of fractured blocks along the pre-existing discontinuities plays an increasingly dominant role during the failure process.

Figure 9b shows the evolution of deviatoric fabric for the contacts only transmitting compressive forces with axial strain in compression tests. It is evident that the increasing rate of deviatoric fabric, for the group where contacts only transmit compressive forces, starts to slow down as the initial joint intensity increases. In fact, the highly jointed rock structure effectively damps the contact intensity and microstructure evolution. After the peak, Fig. 9b also shows a sudden decrease of the deviatoric fabric in intact, 1V + 2H, and 2V + 3H samples corresponding to degradation or collapse of the compressive contact network. Similar to all engaged contacts, deviatoric fabrics of compressive contacts approach their peak values and then gradually decrease with the increase of axial strain to ultimate values in 3V + 5H and 6V + 9H samples.

The deviatoric fabric for contacts that transmits only tensile forces is initially highly anisotropic, and this anisotropy reduces during compressive loading (see Fig. 9c). It is worth noting that the deviatoric fabric of tensile contacts is generally much larger than that of the compressive

contacts in all five cases, which is in agreement with previous numerical observations on high-porosity sandstones by Wu et al. [70]. The “tensile contacts” major principal fabrics is horizontal as a result of the Poisson effect [8], leading to the breakage of more bonds in the horizontal direction and a reduction of the “tensile contacts” anisotropy. This, however, corresponds to an increase in “bonded contacts” anisotropy.

For bonded contacts, the deviatoric fabric experiences a short period of initial decrease as the model is being compacted (see Fig. 9d). The deviatoric fabric then begins to increase at a slow rate to a maximum value which is dependent on the initial joint frequency. Generally, when the amount of fracturing is large, a significant amount of particle rearrangement takes place resulting in large deviatoric fabric values.

In particular, the deviatoric fabric for bonded contacts in the intact rock sample increases rapidly to the largest value among all investigated joint configurations, due to the occurrence of the most intense microcracking activities associated with catastrophic failure of the internal structure. It correlates reasonably well with that of the brittle behavior. Nevertheless, only a slight increase in deviatoric fabric for bonded contacts is observed for 6V + 9H sample. This is attributed to the fact that with the increased density of initial joints, the number of fractures significantly reduced. As a result, cohesion and interparticle restriction are largely maintained, which suppresses particle motion during the compressive loading. Hence, particle orientation is less likely to be random, leading to a lower anisotropy in highly jointed samples.

The coordination number is calculated using the number of particles (N_p) and their contacts (N_c), as expressed below:

$$C_n = 2 \frac{N_c}{N_p} \quad (31)$$

The evolution of the coordination number as a function of axial strain (ϵ_a) under different initial jointing conditions is presented in Fig. 10. It reveals that for the “all contacts” coordination number there is an upward trend before reaching the peak state, as a result of the increasing of overlapping between particles under elastic compression, and followed by a descending trend owing to the degradation of contacts and bonds. Moreover, Fig. 10a shows that for the case of “all contacts,” coordination number increases at a slower rate to a maximum value as the degree of initial jointing increases. This difference can be attributed to the fact that the contact state of the intensely jointed rock sample is relatively loose and dispersive, which means that the formation of an effective force transmission structure and a connected interaction network is prevented.

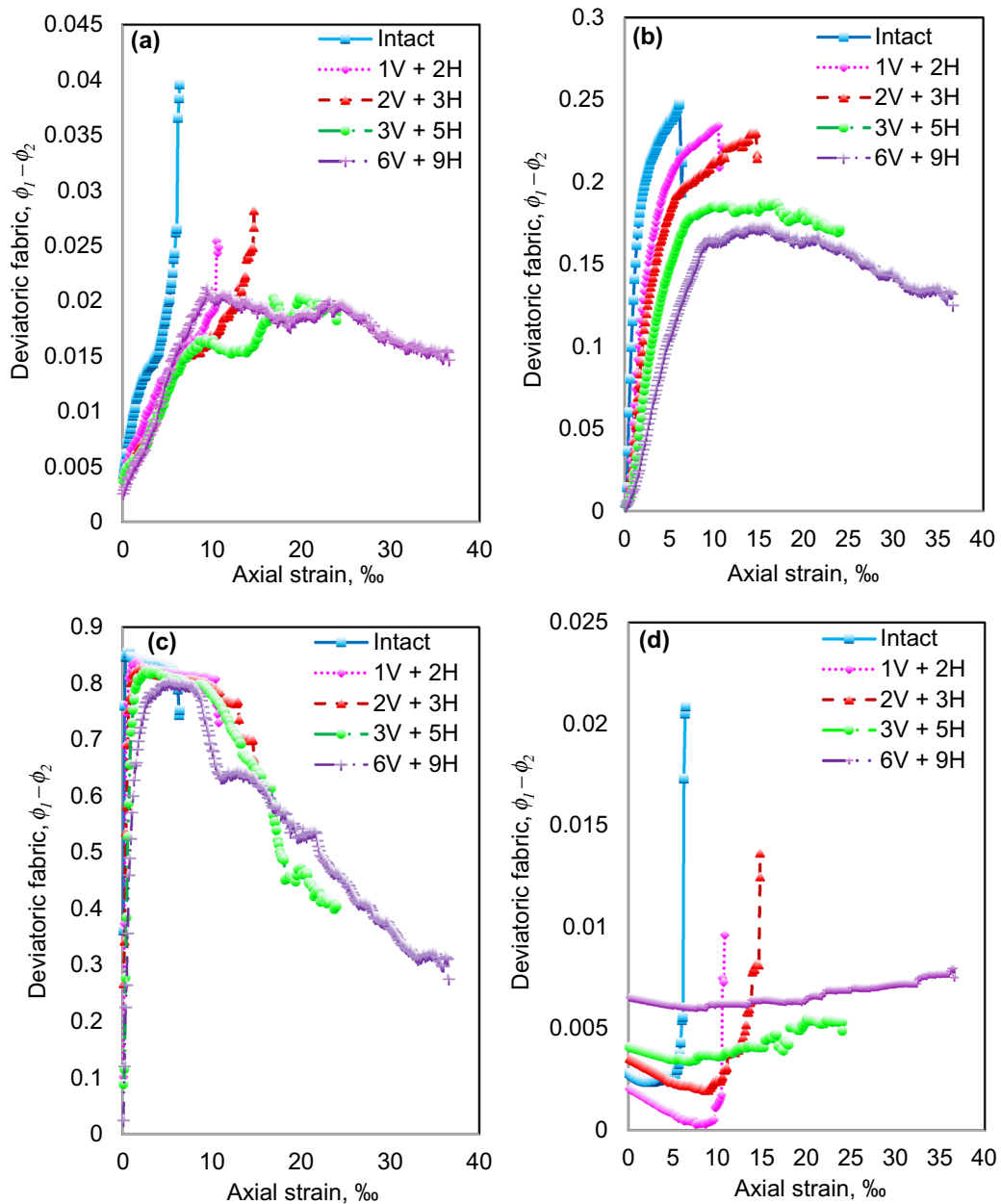


Fig. 9 The deviatoric fabric in the intact and jointed rock samples: **a** considering all engaged contacts; **b** considering only contacts transmitting compressive forces; **c** considering only contacts transmitting tensile forces; **d** considering bonded contacts

For highly jointed rocks, contact force chains are more likely to reach the limiting value for sliding along the pre-existing joints; hence, the decrease in the coordination number (or the loss of contact) is more gradual. The rate of increase or decrease in coordination number is closely related to the tendency of a particulate assemblage to dilate or contract as shown in Fig. 3f.

The coordination number of parallel bonds stays constant at the elastic deformation stage and then starts to decrease when ϵ_a reaches 4.48, 9.78, 10.59, 12.21, and

14.28 % for intact and jointed 1V + 2H, 2V + 3H, 3V + 5H, and 6V + 9H samples, respectively. This observation is in accordance with the fracturing behavior, where the increment of micro-cracks and increasing number of particles being debonded are observed; thereafter, the coordination number of parallel bonds decreases significantly.

The late reduction in coordination number can further confirm the failure mode associated with brittle–ductile transition. This is due to the fact that with the increase in

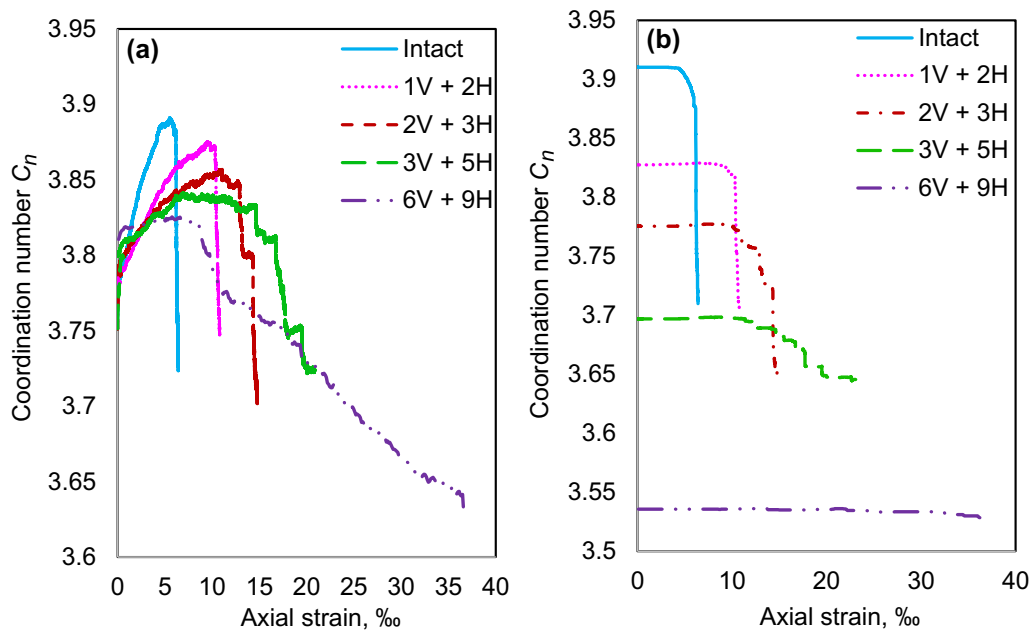


Fig. 10 The coordination number in the intact/jointed rock samples: **a** considering all engaged contacts; **b** considering all bonded contacts

initial joint frequency, the frictional movements of particles on the joint planes are facilitated. It is noted that the increase of the degree of initial jointing prevents further increase of interlocking due to a growing number of particles being debonded, marked out by decreasing initial coordination number of parallel bonds (see Fig. 10b).

3.2.2 Microstructure anisotropy

In quantifying anisotropy in a granular assembly, two anisotropy sources are distinguished: geometrical anisotropy and mechanical anisotropy [26, 46, 75].

Geometrical anisotropy is defined as the local orientation of a contact plane that gives rise to the global anisotropic phenomenon. Mechanical anisotropy is mainly caused by external forces and depends on the induced contact forces in relation to contact plane orientations [76]. For an assembly of circular particles, geometrical anisotropy can be expressed using the distribution of contact normal vectors.

The probability density function $E(\mathbf{n})$ of contact normal at a unit circle in 2D is introduced to identify the likelihood that a contact will have an orientation described by the unit normal vector \mathbf{n} .

$$\int_{\Theta} E(\mathbf{n})d\Theta = 1 \tag{32}$$

Therefore, the fabric tensor of contact normals can be represented as [6]:

$$\Phi_{ij} = \int_{\Theta} E(\mathbf{n})n_i n_j d\Theta = \frac{1}{N_c} \sum_{N_c} n_i n_j \tag{33}$$

The probability density function $E(c)$ can be fitted using a Fourier series in tensorial form as

$$E(\Theta) = \frac{1}{2\pi} \left[1 + a_{ij}^c n_i n_j + a_{ijkl}^c n_i n_j n_k n_l \right] \tag{34}$$

where odd ordered tensors do not contribute to the series solution in terms of the symmetry of the directional data. With a second-order Fourier expansion of $E(c)$, i.e., $E(\Theta) = \frac{1}{2\pi} \left[1 + a_{ij}^c n_i n_j \right]$, substituting into Eq. (33) and

integrating, we get:

$$\Phi_{ij} = \frac{1}{2} \delta_{ij} + \frac{a_{ij}^c}{4} \tag{35}$$

where δ_{ij} is the Kronecker delta; the second-order tensor a_{ij}^c is deviatoric and symmetric and characterizes the fabric anisotropy. In a nutshell, a_{ij}^c can be represented with respect to the deviatoric fabric tensor Φ'_{ij} given by Eq. (35).

$$a_{ij}^c = 4\Phi'_{ij} \tag{36}$$

The mechanical anisotropy can be split into normal force anisotropy (caused by normal contact forces) and tangential force anisotropy (induced by tangential contact forces), which are, respectively, defined as follows [26, 56]:

$$\chi_{ij}^n = \frac{1}{2\pi} \int_{\Theta} \bar{f}^n(\Theta) n_i n_j d\Theta = \frac{1}{N_c} \sum_{c \in N_c} \frac{f^n n_i n_j}{1 + a_{kl}^c n_k n_l} \quad (37)$$

$$\bar{f}^n(\Theta) = \bar{f}^0 [1 + a_{ij}^n n_i n_j] \quad (38)$$

and

$$\chi_{ij}^t = \frac{1}{2\pi} \int_{\Theta} \bar{f}^t(\Theta) t_i n_j d\Theta = \frac{1}{N_c} \sum_{c \in N_c} \frac{f^t t_i n_j}{1 + a_{kl}^c n_k n_l} \quad (39)$$

$$\bar{f}_i^t(\Theta) = \bar{f}^0 [a_{ik}^t n_k - (a_{kl}^t n_k n_l) n_i] \quad (40)$$

where

$$a_{ij}^n = 4 \frac{\chi_{ij}^n}{\bar{f}^0}, \quad a_{ij}^t = 4 \frac{\chi_{ij}^t}{\bar{f}^0} \quad (41)$$

Similar to the previous cases, $\bar{f}^0 = \chi_{ii}^n$ is the average normal force calculated over different Θ and may differ from the average normal force \bar{f} over all contacts.

Collectively, the three anisotropic tensors, a_{ij}^c , a_{ij}^n and a_{ij}^t , are defined to characterize the anisotropic behavior. Because all three tensors are deviatoric in nature, the deviatoric invariants are then used to quantify the degree of anisotropy, given as [26]:

$$a_* = \text{sign}(S_r) \sqrt{\frac{1}{2} a_{ij}^* a_{ij}^*} \quad (42)$$

where the sub-/superscript * stands for *c*, *n* or *t*, corresponding to one of the three cases of anisotropy mentioned above, respectively.

S_r is defined in Eq. (42), and more details can be found in Guo and Zhao [26].

$$S_r = \frac{a_{ij}^* \sigma'_{ij}}{\sqrt{a_{ii}^* a_{kl}^*} \sqrt{\sigma'_{mn} \sigma'_{mn}}} \quad (43)$$

The evolution of anisotropy coefficients of intact and pre-jointed rock samples during confined compressive strength tests is shown in Fig. 11. Although the deviatoric fabric for all engaged contacts is found to be equal to $a_c/2$ [2, 43], the evolution of contact normal anisotropy (a_c) has the same trend as that of deviatoric fabric (Fig. 9a). Hence, there is no need to further discuss the evolution of contact normal anisotropy herein.

The increasing initial joint frequency appears to restrain the growth rate of all anisotropy coefficients. However, the variation of the anisotropy coefficient (a_n) for intact, 1V + 2H, and 2V + 3H rock samples, follows similar manners during rock deformation, the anisotropy coefficients increase with axial strain up to the peak value of around 1.26, 1.23, and 1.22, and then it drops instantaneously to 1.09, 1.13, and 1.14, respectively. Similar to geometric anisotropy (a_c), the variations of the anisotropy coefficient (a_n) for 3V + 5H and 6V + 9H samples

experience a slower progression where the anisotropy coefficients increase to peaks as the loading proceeds and then relaxes to a residual values up to fluctuations of rather small amplitude. In fact, the rise and fall observed in the value a_n during the loading process correspond, respectively, to the generation and collapse of microstructures. For instance, the significant drop of a_n in the intact sample implies that the reduction in a_n coincides with the reduction observed in the rock strength as well as the high level of fracturing. As already explained, this dropping point is in response to the onset of coalescence of pre-existing microcracks and freshly formed fractures into a through-going rupture.

As initial joint frequency intensifies, an abrupt fall after peak in 3V + 5H and 6V + 9H rock samples cannot be observed, instead the variation of a_n fully mobilized at larger axial strain, and the following reduction becomes less significant compared to other samples. This decreasing trend for a_n indicates that the sliding through pre-existing joints in the rock deformation process plays an increasingly governing role by activating large frictional movement of unbroken blocks as well as the high degree of dilation until the intact material failure mode is entirely replaced. Compared with the other mechanical anisotropy a_n , the tangential force anisotropy a_t during the loading course is obviously smaller.

It is worth noting although this rapid rise of mechanical anisotropy can be observed for all cases, the growth rate is still significantly reduced with the degree of initial jointing, because the assembly is kinematically locked initially and deforms elastically; however, the highly jointed rock structure effectively damps the granular dynamics and contact intensity as stated by Zhao et al. [82, 83]. In general terms, this rapid rise of the anisotropies of contact tangential force a_t corresponds to the development of frictional resistance as a result of the relative translational movement of particles. The variation of anisotropy coefficient a_t is analogous to what happens with the normal contact force a_n for intact, 1V + 2V, and 2V + 3H rock samples, which it reaches a peak value at a finite axial strain and then it accompanies an abrupt drop, indicating that the large rise of bond breakage as well as the reduction of contact density leads to particles gaining rotational freedom; as a result, tangential forces are slowly released.

In contrast to a_n for the 3V + 5H and 6V + 9H rock samples, variation of a_t acts in a different manner where it continuously increases with axial strain up to the end of the test without any onset of decreasing. This may be attributed to the fact that the rotational mobility of the particles is strongly reduced as a result of tightly connected structure due to much lower fracturing intensity so that the largely bonded particles tend to slide rather than rolling with a strong increase of friction mobilization. Indeed, it further

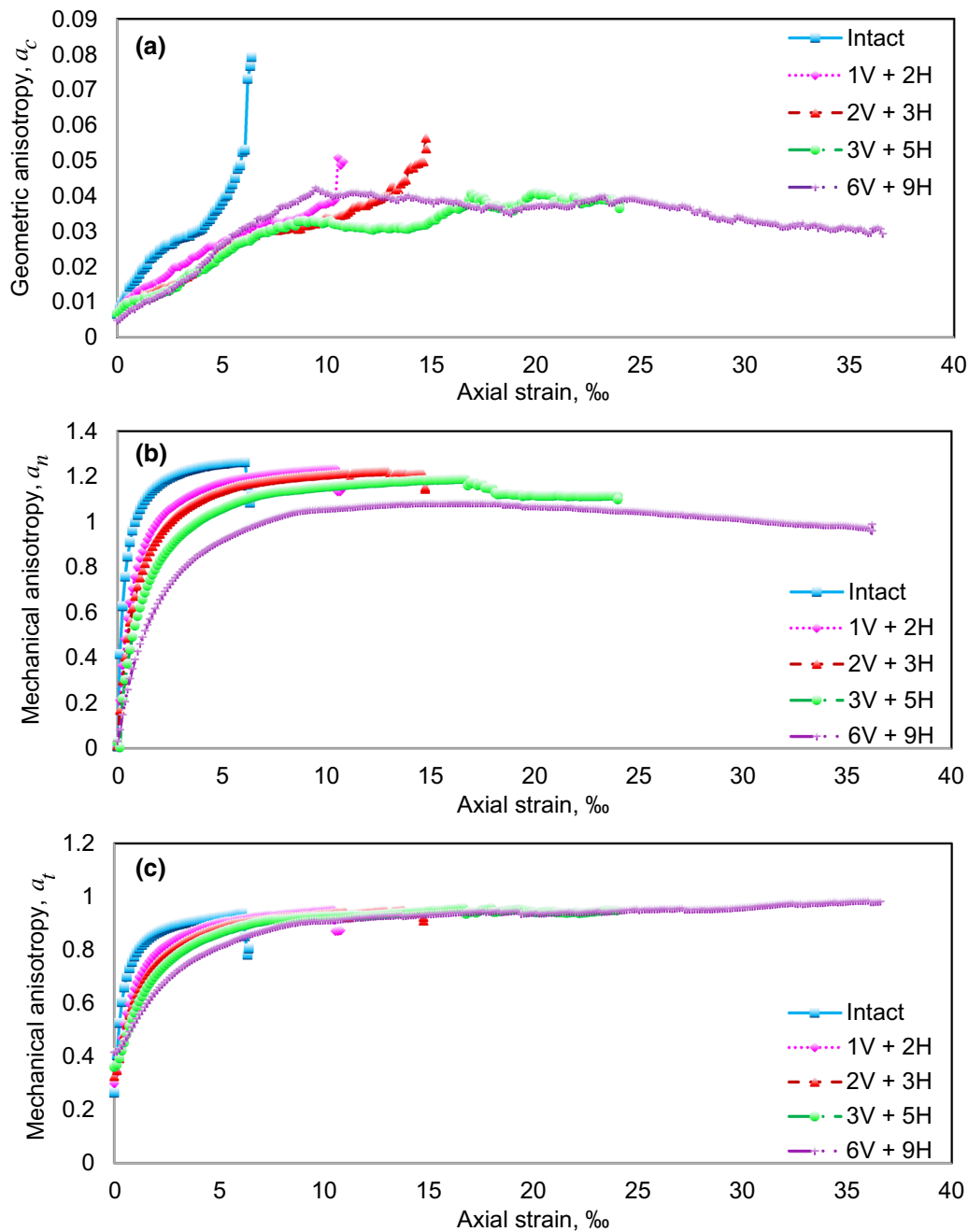


Fig. 11 a–c Evolution of geometrical anisotropy a_c , mechanical anisotropy a_n , and mechanical anisotropy a_t as a function of cumulative axial strain in intact and jointed rock samples

confirms that as the governing failure mechanism is progressively transitioned from mix failure mode to sliding through pre-existing discontinuities with the increasing degree of initial jointing, the level of friction mobilization, which reflects the dependence of the mechanical stability of the material on friction forces, also increases. Nevertheless, this a_t increase is not large enough to additively compensate for the decrease of a_c and a_n , so that the shear strength continues to exhibit a softening trend.

3.2.3 Anisotropic distribution

Given the preceding picture of the anisotropy evolutions under different joint configurations for confined compression tests, further examination of the polar distributions of the geometric and mechanical anisotropies in terms of micro-structural mechanism can provide a better description of the complex macroscopic behavior including the topology of arrangement of particles as well as the internal

force transmissions. Therefore, the polar distributions of anisotropies of fabric, contact normal, and shear forces at three distinct (initial, peak, and 50% post-peak) states for the intact, 2V + 3H, and 6V + 9H samples are selected to reflect microstructural changes during the rock deformation, of which failure mechanisms are governed by intact rock failure, mixed failure, and sliding through pre-existing joints, respectively. In addition, the numerically measured data are presented together with the approximations to the distributions using second-order tensorial relationships (34), (38), and (40). This second-order tensorial relationship has been widely applied to quantify the spatial orientations of micro-mechanical descriptors, such as contact normals [33, 60] and contact forces [46]. Figures 12–14 show that the approximations appear to visually well-represent the numerically measured data and the initial anisotropy condition totally evolves due to the induced anisotropy within intact and pre-jointed samples. More precisely, compared to the polar distributions of mechanical anisotropies, the polar histograms of contact normals seem to have approximately a circular form during the loading process as a result of the value of contact normal anisotropy is far below than 1, as suggested by Hosseininia [29, 30] that the circle deforms as a peanut when the value of a_c increases and closes to 1, indicating a high degree of anisotropy. Nevertheless, polar histograms for the intact samples during the deformation process are observed to be more elongated along the loading axis due to interparticle contacts being disintegrated reflected by the relatively marked rise of anisotropy.

The polar histogram of contact normal force for the selected three samples at the initial state seems to have approximately a circular form, which reveals that the magnitude of average contact normal force is almost the same in all directions (see Fig. 12). This is expected since all samples were initially compacted under isotropic condition. The histograms, however, are elongated, at the peak stress state (see Fig. 13), along the loading axis and slimed along the horizontal direction for the intact rock samples. In addition, the long axis of histograms for jointed samples is increasingly deviated anticlockwise from the loading axis with the higher level of initial jointing. This evolution in the normal force anisotropy distribution suggests the development of new contacts and the increase in the magnitude of normal forces along the loading axis in relation to those in the horizontal direction are largely affected by the increased initial joint frequency. After the entire loading course, the anisotropies of contact normal forces decrease rapidly accompanied by the significant rotation of its orientations, particularly for 6V + 9H samples (see Fig. 14). The reduction in contact normal force anisotropy is related to reorganization of microstructure when the dilation is intense. Dilation is

initiated by movement of highly compressed conglomerates of particles that move as rigid blocks and disrupt the assembly; therefore, the 6V + 9H samples characterized by the highest dilatant activity show the lowest degree of contact normal force anisotropy as well as the continuous decreasing trend.

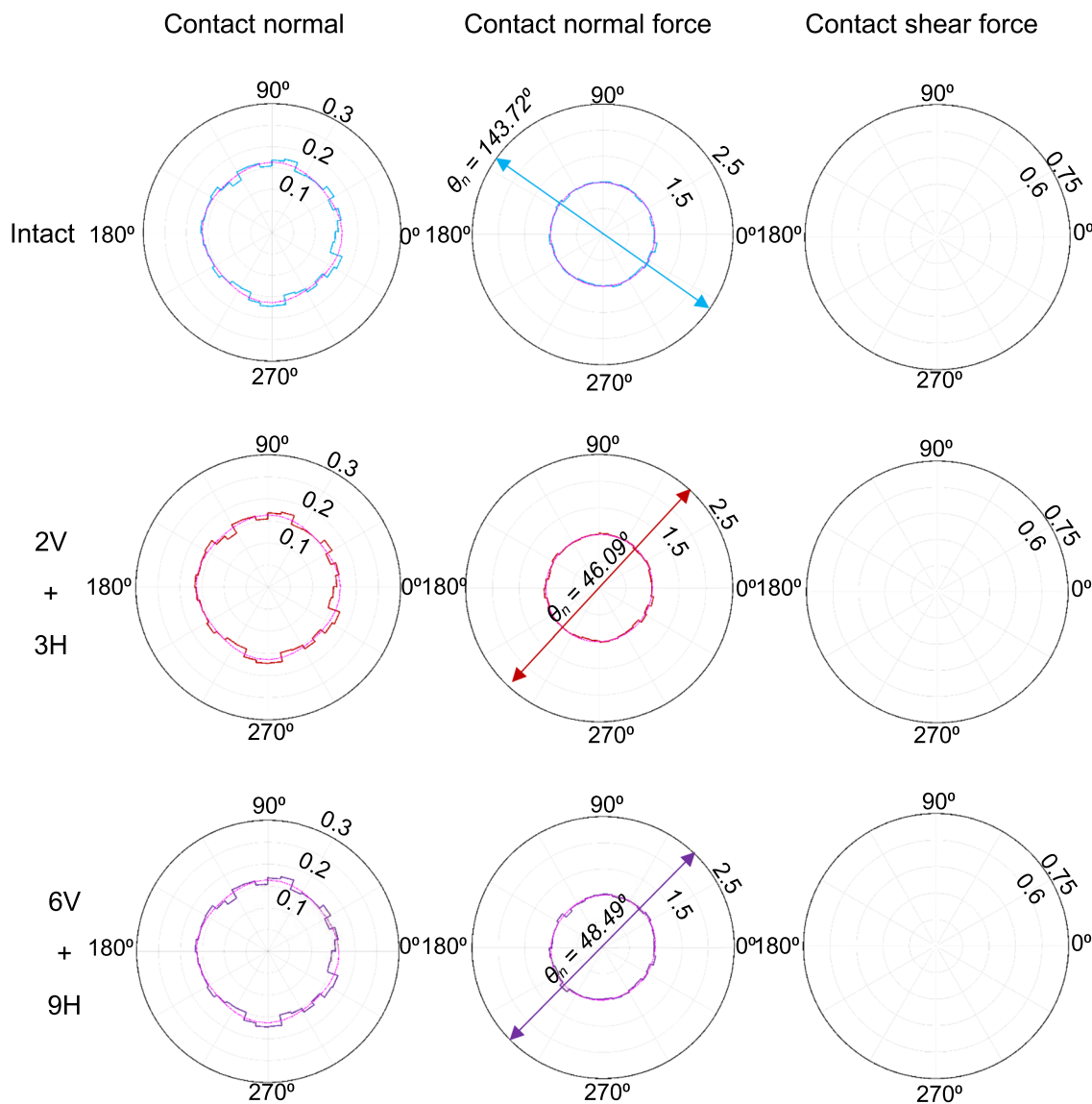
The initial contact tangential force inside all the samples is close to zero, because the initial loading relates to an isotropic compaction and no shear deformation occurs. As a consequence, no shear stress is mobilized among particles. For the peak stress state, however, it is observed that the polar histograms of tangential forces are paraded by four leaps instead of having a peanut-like form such as happened for contact normal force distribution. The reason explained by Hosseininia [29] is that the direction of the contact tangential force is perpendicular to the contact normal force, and thus, the distribution of tangential contact force differs.

Analogous to what happens with the contact normal force, the principal direction of tangential force anisotropy (θ_t) rapidly orients along loading axis ($\theta_t = 90^\circ$) for the intact rock samples, while it is inclined around 3 and 9 degrees anticlockwise with respect to the loading axis for 3V + 5H and 6V + 9H rock samples at peak stress state; subsequently, it is rotated counter-clockwise by approximately 5° and 13° with respect to the loading axis when it reaches the 50% post-peak stress state. This can be attributed to the fact that the orientations of joint sets within the assemblies strongly influence the direction of maximum mobilized shear stress. In addition, by comparing the variation of θ_t with that of θ_n at the peak and post-peak stress states, it is observed that the principal directions of contact force and fabric anisotropies are essentially coincident. The explanation for this observation is that distribution of contacts is defined by contacts that actively transmit force; then, the coincidence of contact force and fabric tensors is assured [6].

4 Discussion

4.1 Macro-scale response and microscopic origin

Based on a detailed 2D DEM analysis, better understanding of how the rock mass responds to the increase in the intensity of initial joints has been achieved. From the macroscopic point of view, the level of such weakness planes influences the mechanical characteristics of the rock mass through: (i) a reduction in stiffness and peak stress, (ii) brittle–ductile transition, (iii) less accentuated post-peak stress drops, (iv) decrease in microcracking intensity (Fig. 3), (v) shift in failure modes, and (vi) variations of



Note: - - - indicates the second-order tensorial approximations to the distributions.

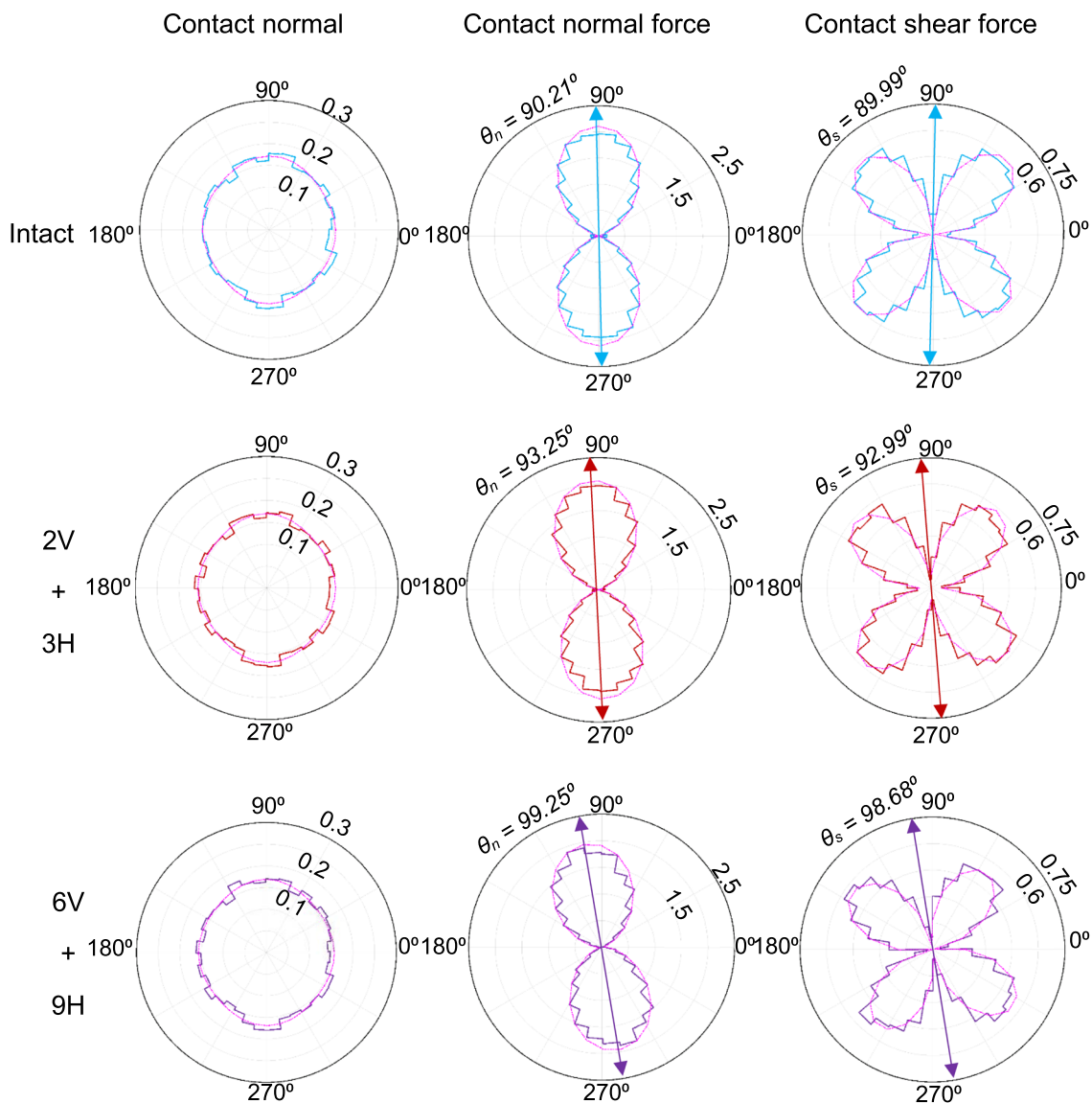
Fig. 12 Distribution of anisotropies of contact normal, normalized average contact normal force ($\bar{f}^n(\theta)/\bar{f}^0$), and normalized average contact shear force ($\bar{f}_t^s(\theta)/\bar{f}^0$) of the intact and two jointed rock samples at initial stress state

orientation distributions of microtensile and shear cracks (Fig. 4).

The above effects on the mechanical behavior are also manifested in the energy budget spent during rock deformation. The addition of further jointing to the sample weakens the rock brittleness nature and leads to the less intense fracturing in the microstructure, which, from the viewpoint of energy, makes the energy storage capacity lower, while the energy dissipation capacity of the rock becomes higher. This prohibits strain energy accumulation and facilitates friction dissipation (Fig. 8).

The fracturing activity, which itself only dissipates a negligible amount of input energy (Table 6 and Fig. 8),

imparts permanent changes to the solid microstructure that can be delineated by the enhanced deviator fabric (Fig. 9d) and the reduced coordination number below the initial state (Fig. 10b). It is worth noting that the change in both the deviator fabric and coordination number for bonded contacts has been significantly affected by the increase in initial joint intensity. This observation is due to the fact that the decrease in the amount of fracturing leads to more particles remain bonded. Consequently, particles may survive in the fabric rearrangement process as a result of the slow release of inter-particle constraints and the change in both deviator fabric and coordination number is significantly reduced.



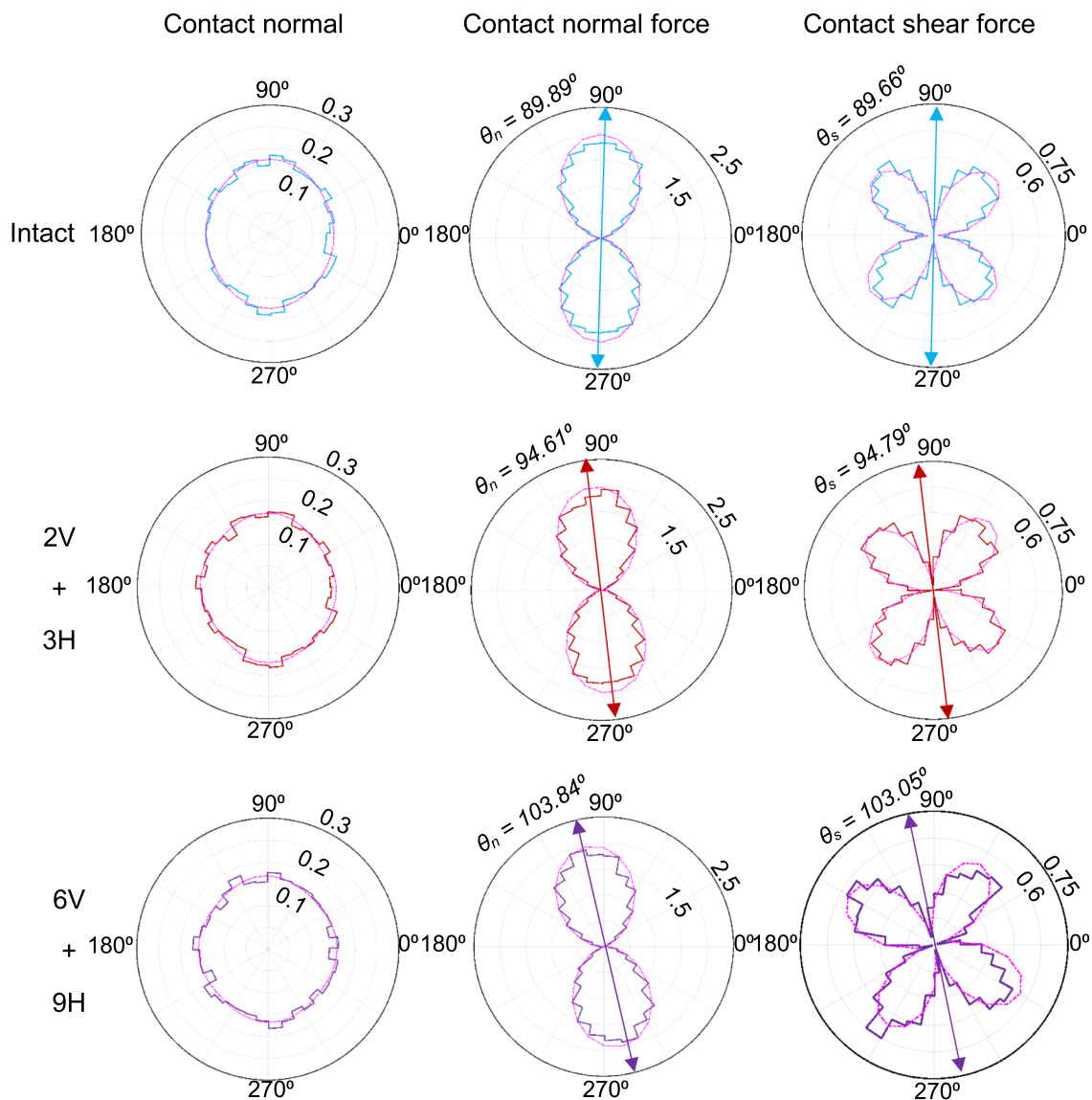
Note: - - - indicates the second-order tensorial approximations to the distributions.

Fig. 13 Distribution of anisotropies of contact normal, normalized average contact normal force ($\bar{f}^n(\theta)f^0$), and normalized average contact shear force ($\bar{f}_t^s(\theta)f^0$) of the intact and two jointed rock samples at peak stress state

Further insights have been gained by examining the development of particle kinematics, shear strain, void ratio, and force chain distributions in intact and pre-jointed samples, which are not easily visualized in experiments or continuum models. It has been found that in an intact sample, the macroscopic rupture surface exhibits a high concentration of shear strains and a large amount of translational and rotational granular temperatures (Fig. 6). With increasing initial joint frequency, many isolated zones of strain localization are observed, yet they fail to form a connected zone. Therefore, no catastrophic failure associated with macro-failure planes traversing the entire sample is formed. In particular, neither apparent localized

patterns of shear strain nor granular temperatures can be found in 6V + 9H samples. This is due to the sliding that develops on pre-existing discontinuity being the dominant failure mechanism as a result of large plastic deformation (Fig. 3) occurring without crack nucleation.

From a micromechanical standpoint, the strengths of intact and pre-jointed samples depend on its ability to develop anisotropies. The trend found for the mechanical anisotropies (see Fig. 11) is generally synchronized with that for the macroscopic stress observed in Fig. 3, which was also reported in several laboratory and numerical studies [6, 26, 45].



Note: ----- indicates the second-order tensorial approximations to the distributions.

Fig. 14 Distribution of anisotropies of contact normal, normalized average contact normal force ($\bar{f}^n(\theta)f^0$), and normalized average contact shear force ($\bar{f}_t^s(\theta)f^0$) of the intact and two jointed rock samples at 50% post-peak stress state

With the increase in initial joint frequency, the rock sample behaves in a more brittle-ductile fashion with less prominent post-peak stress (see Fig. 3) and progressive transition to sliding failure mode along the joint planes (Figs. 4 and 6). This evolution of macroscopic deformation can be traced back to the micromechanical origins where a softening trend of the contact normal force anisotropy is compensated by a gradual increase of the tangential force anisotropy instead of significant falloffs of the both mechanical anisotropies. This further confirms the addition of further jointing to the sample leads to an increasing dominance of the sliding failure mode on the rock deformation; thus, a strong activation of tangential forces is

ensured to balance the increasing mobilization of friction forces [2, 6].

4.2 Limitation and future outlook

Discrete element modeling of grain-scale heterogeneity, i.e., particle size distribution or non-spherical distinct element, plays an important role in controlling its emergent macroscopic response under compression. However, no matter which particle size distribution or grain shape is used, it is necessary to re-calibrate the values of the micro-mechanical parameters used in the analysis to match the measured macro-mechanical behavior. This means that

when the arrangement of the spherical particles changes, some self-adjustment of the micro-mechanical parameters takes place to produce the expected macro-mechanical behavior [17, 27]. Therefore, the main trends related to the addition of joints on the strength and deformability of the rock samples remain essentially the same even though some slight changes on the exact values are possible.

Substantial insights have already been gained from discrete element numerical modeling of acoustic emissions (AEs) in progressive mechanisms of rock failure [28, 59, 79, 80]. In particular, acoustic emissions result from sources of internal damage due to sudden local dislocations in the form of tensile or shear microcracks can foster a deeper understanding of the onset and propagation of microcracking and provide significant additional information to complement micromechanical study to analyze fracture growth mechanisms and their correlation with increasing level of initial jointing.

5 Conclusion

The deformability and failure behavior (progressive fracture growth, material damage, failure) of intact rock and rock samples containing two sets of persistent joints with increased initial joint frequency has been investigated through confined compression tests by discrete element numerical simulation. The smooth-joint contact model and the linear parallel-bond model were selected in the numerical model for the pre-existing joints and the rock matrix, respectively. The entire deformation and failure process are visually represented, and the failure mode in reasonable accordance with experimental results is obtained. The results show that the failure mechanism is much affected by the degree of initial jointing. The following preliminary conclusions can be drawn from the numerical tests:

1. As the density of the initial jointing increases, the rock deformation behaves in a more brittle-ductile fashion with corresponding patterns of visible strain hardening, reduced stress drops and fracturing activities, and dispersed microcracking distribution. This is generally synchronized with transition of failure mode to joint slip yielding mechanism leading to the absence of nucleation and coalescence of fractures as a consequence of the movement of conglomerates of particles along the joint plane.
2. The relative contributions of the elastic energies to the energy budget and to the fracture energy are found to decline with the increase in initial joint intensity. This is compatible with the fact the frictional energy dissipation gradually prevails over the elastic strain

energies build-up as a result of the sliding along the joint plane.

3. With the increase in initial joint intensity, rock samples are prevented from developing larger fabric and force anisotropies, which further result in a smaller macroscopic peak strength.
4. Consistent with the macroscopic deformation behavior, i.e., stress–strain curve, the variations of geometric and mechanical anisotropies provide micromechanical evidence that a transition from brittle to ductile behavior occurs with increasing initial joint frequency.

Acknowledgement This research is supported by the Natural Sciences and Engineering Research Council of Canada (NSERC). Financial support provided by McGill Engineering Doctoral Award (MEDA) to the first author is appreciated.

References

1. Alejano LR, Arzúa J, Bozorgzadeh N, Harrison JP (2017) Tri-axial strength and deformability of intact and increasingly jointed granite samples. *Int J Rock Mech Min Sci* 95:87–103
2. Azéma E, Radjai F, Dubois F (2013) Packings of irregular polyhedral particles: strength, structure, and effects of angularity. *Phys Rev E* 87(6):062203
3. Bahaaddini M, Hagan PC, Mitra R, Hebblewhite BK (2015) Parametric study of smooth joint parameters on the shear behaviour of rock joints. *Rock Mech Rock Eng* 48(3):923–940
4. Bahaaddini M, Hagan PC, Mitra R, Hebblewhite BK (2016) Numerical study of the mechanical behaviour of non-persistent jointed rock masses. *Int J Geomech* 16:04015035
5. Bahaaddini M, Sharrock G, Hebblewhite BK (2013) Numerical investigation of the effect of joint geometrical parameters on the mechanical properties of a non-persistent jointed rock mass under uniaxial compression. *Comput Geotech* 49:206–225
6. Bathurst RJ, Rothenburg L (1990) Observations on stress-force-fabric relationships in idealized granular materials. *Mech Mater* 9(1):65–80
7. Brown ET, Trollope DH (1970) Strength of a model of jointed rock. *ASCE J Soil Mech Found Div Proc* 1970:685–704
8. Cheung LYG, O'Sullivan C, Coop MR (2013) Discrete element method simulations of analogue reservoir sandstones. *Int J Rock Mech Min Sci* 63:93–103
9. Chen X, Zhang SF, Cheng C (2018) Numerical study on effect of joint strength mobilization on behavior of rock masses with large nonpersistent joints under uniaxial compression. *ASCE Int J Geomech* 18(11):04018140(1)–04018140(21)
10. Chiu CC, Wang TT, Weng MC, Huang TH (2013) Modeling the anisotropic behavior of jointed rock mass using a modified smooth-joint model. *Int J Rock Mech Min Sci* 62:14–22
11. Cho N, Martin CD, Sego DC (2007) A clumped particle model for rock. *Int J Rock Mech Min Sci* 44(7):997–1010
12. Cundall PA, Strack ODL (1979) A discrete numerical model for granular assemblies. *Géotechnique* 29(1):47–65
13. Dinç O, Scholtès L (2018) Discrete analysis of damage and shear banding in argillaceous rocks. *Rock Mech Rock Eng* 51:1521–1538
14. Duan K, Kwok CY, Tham LG (2015) Micromechanical analysis of the failure process of brittle rock. *Int J Numer Anal Meth Geomech* 39(6):618–634

15. Duan K, Kwok CY, Ma X (2017) DEM simulations of sandstone under true triaxial compressive tests. *Acta Geotech* 12:495–510
16. Eshiet KII, Sheng Y (2016) The role of rock joint frictional strength in the containment of fracture propagation. *Acta Geotech* 12:897–920
17. Fan X, Kulatilake PHSW, Chen X (2015) Mechanical behavior of rock-like jointed blocks with multi-non-persistent joints under uniaxial loading: a particle mechanics approach. *Eng Geol* 190:17–32
18. Feng P, Dai F, Liu Y, Xu NW, Du HB (2019) Coupled effects of static-dynamic strain rates on the mechanical and fracturing behaviors of rock-like specimens containing two unparallel fissures. *Eng Fract Mech* 207:237–253
19. Fu JW, Liu SL, Zhu WS, Zhou H, Sun ZC (2018) Experiments on failure process of new rock-like specimens with two internal cracks under biaxial loading and the 3-D simulation. *Acta Geotech* 13(4):853–867
20. Gao G, Meguid MA (2018) Modeling the impact of a falling rock cluster on rigid structures. *ASCE Int J Geomech* 18(2):1–15
21. Gao G, Meguid MA (2018) On the role of sphericity of falling rock clusters—insights from experimental and numerical investigations. *Landslides* 15(2):219–232
22. Gao G, Meguid MA (2018) Effect of particle shape on the response of geogrid-reinforced systems: insights from 3D discrete element analysis. *Geotext Geomembr* 46(6):685–698
23. Garcia FE, Bray JD (2018) Distinct element simulations of earthquake fault rupture through materials of varying density. *Soils Found* 58(4):986–1000
24. Ghazvinian A, Sarfarazi V, Schubert W, Blumel M (2012) A study of the failure mechanism of planar non-persistent open joints using PFC2d. *Rock Mech Rock Eng* 45:677–693
25. Glynn EF, Veneziano D, Einstein HH (1978) The probabilistic model for shearing resistance of jointed rock. In: *Proceedings of the 19th US symposium on rock mechanics*, Stateline, Nevada, pp 66–76
26. Guo N, Zhao JD (2013) The signature of shear-induced anisotropy in granular media. *Comput Geotech* 47:1–15
27. Hatzor YH, Palchik V (1997) The influence of grain size and porosity on crack initiation stress and critical flaw length in dolomites. *Int J Rock Mech Min Sci* 34:805–816
28. Hazzard JF, Young RP (2000) Simulating acoustic emissions in bonded-particle models of rock. *Int J Rock Mech Min Sci* 37(5):867–872
29. Hosseininia ES (2012) Investigating the micromechanical evolutions within inherently anisotropic granular materials using discrete element method. *Granul Matter* 14:483–503
30. Hosseininia ES (2013) Stress-force-fabric relationship for planar granular materials. *Géotechnique* 63:830–841
31. Huang F, Shen J, Cai M, Xu CS (2019) An empirical UCS model for anisotropic blocky rock masses. *Rock Mech Rock Eng* 52:3119
32. Hurley RC, Hall SA, Andrade JE, Wright J (2016) Quantifying interparticle forces and heterogeneity in 3D granular materials. *Phys Rev Lett* 117:098005
33. Kanatani K (1984) Distribution of directional data and fabric tensors. *Int J Eng Sci* 22:149–164
34. Kulatilake PHSW, He W, Um J, Wang H (1997) A physical model study of jointed rock mass strength under uniaxial compressive loading. *Int J Rock Mech Min Sci* 34(3):165.e1–165.e15
35. Kulatilake PHSW, Liang J, Gao H (2001) Experimental and numerical simulations of jointed rock block strength under uniaxial loading. *J Eng Mech* 127(12):1240–1247
36. Itasca Consulting Group (2014) Particle flow code in three dimensions (PFC2D 5.0), Minneapolis
37. Li X, Konietzky H, Li XB, Wang Y (2019) Failure pattern of brittle rock governed by initial microcrack characteristics. *Acta Geotech* 14:1437–1457
38. Liu J, Wautier A, Bonelli S, Nicot F, Darve F (2020) Macroscopic softening in granular materials from a mesoscale perspective. *Int J Solids Struct* 193–194:222–238
39. Lois G, Lemaître A, Carlson J (2007) Spatial force correlations in granular shear flow. I. Numerical evidence. *Phys Rev E* 76(2):021302
40. Løvoll G, Måløy KJ, Flekkøy EG (1999) Force measurements on static granular materials. *Phys Rev E* 60(5):5872
41. Ma G, Regueiro RA, Zhou W, Liu J (2018) Spatiotemporal analysis of strain localization in dense granular materials. *Acta Geotech* 14(4):973–990
42. Ma G, Regueiro RA, Zhou W, Wang Q, Liu J (2018) Role of particle crushing on particle kinematics and shear banding in granular materials. *Acta Geotech* 13(3):601–618
43. Ma G, Zhou W, Ng TT, Cheng YG, Chang XL (2015) Microscopic modeling of the creep behavior of rockfills with a delayed particle breakage model. *Acta Geotech* 10(4):481–496
44. Mas Ivars D, Pierce ME, Darcel C, Reyes-Montes J, Potyondy DO, Young RP, Cundall PA (2011) The synthetic rock mass approach for jointed rock mass modelling. *Int J Rock Mech Min Sci* 48(2):219–244
45. Rothenburg L, Bathurst RJ (1989) Analytical study of induced anisotropy in idealized granular materials. *Géotechnique* 39:601–614
46. Ouadfel H, Rothenburg L (2001) ‘Stress–force–fabric’ relationship for assemblies of ellipsoids. *Mech Mater* 33:201–221
47. Park B, Min KB (2015) Bonded-particle discrete element modeling of mechanical behavior of transversely isotropic rock. *Int J Rock Mech Min Sci* 76:243–255
48. Potyondy DO, Cundall PA (2004) A bonded-particle model for rock. *Int J Rock Mech Min Sci* 41(8):1329–1364
49. Prudencio M, Van Sint Jan M (2007) Strength and failure modes of rock mass models with non-persistent joints. *Int J Rock Mech Min Sci* 44(6):890–902
50. Quiñones J, Arzúa J, Alejano LR, García-Bastante F, Mas Ivars D, Walton G (2017) Analysis of size effects on the geomechanical parameters of intact granite samples under unconfined conditions. *Acta Geotech* 12:1229–1242
51. Satake M (1978) Constitution of mechanics of granular materials through graph representation. In: *Proceedings of the 26th Japanese national congress of theoretical and applied mechanics*, pp 257–66
52. Scholtès L, Donzé FV (2012) Modelling progressive failure in fractured rock masses using a 3D discrete element method. *Int J Rock Mech Min Sci* 52:18–30
53. Shang J, West LJ, Hencher SR, Zhao Z (2018) Geological discontinuity persistence: implication and quantification. *Eng Geol* 241:41–54
54. Shang J, West LJ, Hencher SR, Zhao Z (2018) Tensile strength of larger-scale incipient rock joints: a laboratory investigation. *Acta Geotech* 13:869–886
55. Shen WG, Zhao T, Crosta GB, Dai F (2017) Analysis of impact induced rock fragmentation using a discrete element approach. *Int J Rock Mech Min Sci* 98:33–38
56. Shi J, Guo P (2018) Fabric evolution of granular materials along imposed stress paths. *Acta Geotech* 13(6):1341–1354
57. Silbert LE, Grest GS, Landry JW (2002) Statistics of the contact network in frictional and frictionless granular packings. *Phys Rev E* 66(6):061303
58. Singh M, Rao KS, Ramamurthy T (2002) Strength and deformational behaviour of a jointed rock mass. *Rock Mech Rock Eng* 35:45–64

59. Song ZY, Konietzky H, Herbst M (2019) Bonded-particle model-based simulation of artificial rock subjected to cyclic loading. *Acta Geotech* 14:955–971
60. Sun Q, Zheng JX (2019) Two-dimensional and three-dimensional inherent fabric in cross-anisotropic granular soils. *Comput Geotech* 116:103197
61. Vergara MR, Jan MVS, Lorig L (2016) Numerical model for the study of the strength and failure modes of rock containing non-persistent joints. *Rock Mech Rock Eng* 49(4):1211–1226
62. Varela Valdez A, Morel S, Marache A, Hinojosa M, Riss J (2018) Influence of fracture roughness and micro-fracturing on the mechanical response of rock joints: a discrete element approach. *Int J Fract* 213:87–105
63. Vora HB, Morgan JK (2019) Microscale characterization of fracture growth and associated energy in granite and sandstone analogs: insights using the discrete element method. *J Geophys Res Solid Earth* 124:7993–8012
64. Walton G, Alejano LR, Arzua J, Markley T (2018) Crack damage parameters and dilatancy of artificially jointed granite samples under triaxial compression. *Rock Mech Rock Eng* 51:1637–1656
65. Wang J, Gutierrez MS, Dove JE (2007) Numerical studies of shear banding in interface shear tests using a new strain calculation method. *Int J Numer Anal Meth Geomech* 31(12):1349–1366
66. Wang J, Yan HB (2012) DEM analysis of energy dissipation in crushable soils. *Soils Found* 52(4):644–657
67. Wang TT, Huang TH (2009) A constitutive model for the deformation of a rock mass containing sets of ubiquitous joints. *Int J Rock Mech Min Sci* 46(3):521–530
68. Wang Y, Tonon F (2009) Modeling Lac du Bonnet granite using a discrete element model. *Int J Rock Mech Min Sci* 46:1124–1135
69. Wang Y, Tonon F (2010) Discrete element modeling of rock fragmentation upon impact in rockfall analysis. *Rock Mech Rock Eng* 44:23–35
70. Wu H, Guo N, Zhao J (2018) Multiscale modeling and analysis of compaction bands in high-porosity sandstones. *Acta Geotech* 13(3):575–599
71. Xu GW, He C, Chen ZQ, Wu D (2018) Effects of the micro-structure and micro-parameters on the mechanical behaviour of transversely isotropic rock in Brazilian tests. *Acta Geotech* 13:887–910
72. Xu T, Xu Q, Tang C, Ranjith PG (2013) The evolution of rock failure with discontinuities due to shear creep. *Acta Geotech* 8(6):567–581
73. Yang XX, Kulatilake PHSW, Chen X, Jing HW, Yang SQ (2016) Particle flow modeling of rock blocks with nonpersistent open joints under uniaxial compression. *ASCE Int J Geomech* 16(6):04016020
74. Yang XX, Qiao WG (2018) Numerical investigation of the shear behavior of granite materials containing discontinuous joints by utilizing the flat-joint model. *Comput Geotech* 104:69–80
75. Zhao S, Zhou X, Liu W (2015) Discrete element simulations of direct shear tests with particle angularity effect. *Granul Matter* 17(6):793–806
76. Zhao S, Zhou X (2017) Effects of particle asphericity on the macro- and micro-mechanical behaviors of granular assemblies. *Granul Matter* 19(2):38
77. Zhang HQ, Zhao ZY, Tang CA, Song L (2006) Numerical study of shear behavior of intermittent rock joints with different geometrical parameters. *Int J Rock Mech Min Sci* 43:802–816
78. Zhang N, Evans TM (2019) Discrete numerical simulations of torpedo anchor installation in granular soils. *Comput Geotech* 108:40–52
79. Zhang Q, Zhang X (2017) A numerical study on cracking processes in limestone by the b-value analysis of acoustic emissions. *Comput Geotech* 92:1–10
80. Zhang SH, Wu SC, Duan K (2019) Study on the deformation and strength characteristics of hard rock under true triaxial stress state using bonded-particle model. *Comput Geotech* 112:1–16
81. Zhang XP, Wong L (2012) Cracking processes in rock-like material containing a single flaw under uniaxial compression: a numerical study based on parallel bonded-particle model approach. *Rock Mech Rock Eng* 45:711–737
82. Zhao T, Crosta GB, Dattola G, Utili S (2018) Dynamic fragmentation of jointed rock blocks during rockslide-avalanches: insights from discrete element analyses. *J Geophys Res Solid Earth* 123:1–20
83. Zhao Y, Semnani SJ, Yin Q, Borja RI (2018) On the strength of transversely isotropic rocks. *Int J Numer Anal Methods Geomech* 42:1917–1934
84. Zhou C, Xu C, Karakus M, Shen J (2019) A particle mechanics approach for the dynamic strength model of the jointed rock mass considering the joint orientation. *Int J Numer Anal Methods Geomech* 43:2797–2815

Publisher's Note Springer Nature remains neutral with regard to jurisdictional claims in published maps and institutional affiliations.